

Chemical Reaction Dynamics under Vibrational Strong Coupling



Andrew C. Hunt
Pembroke College

A thesis submitted for the Honour School of Chemistry

Part II 2023

Acknowledgements

Deep in the bowels of the PTCL theory wing there lies an oasis of stimulating conversation and hilarious moments, all thanks to some of the most unique and inspiring people I have ever had the pleasure of working alongside.

Firstly, I would like to thank my supervisor David Manolopoulos for his guidance throughout this year. Watching you formulate entire arguments in your head - with clarity only paralleled by the signature handwriting employed in their execution - has truly been incredible. The meetings between you, me and Johan, to which you gave the apt name “*bullshit hour*” will forever be amongst my favorite memories from my time at Oxford - thank you.

If one were to be given the tools to design the perfect mentor they would struggle to recreate someone anywhere near as kind or knowledgeable as Johan Runeson. You have broadened my understanding in physics, rectified many of my mathematical misconceptions and most importantly shown me unwavering patience, for which I can only express my utmost gratitude.

Annina and Seth - I am amazed you have managed to put up with me these past nine months. Thanks for the interesting conversations and teaching me all I know now about the dark arts of FORTRAN77 debugging. Aadi, Andrew, Daniel, Chris and Alex: if I had more space, you too would have paragraphs... Thanks you all for the jokes, thoughts and memories upon which I will forever reminisce.

Finally, to my family and friends of which did not reside with me in the theory wing, thank you for letting me bore you with the latest details of my project, and the support you have given me throughout the ups and downs of this truly epic year.

Summary

In this thesis, we use classical, semi-classical and quantum-mechanical methods to simulate chemical reaction dynamics inside of an optical cavity. Within such a cavity, by selectively coupling vibrational modes of the reactants to the vacuum state of light, recent experiments have observed significant changes in reaction rates and equilibrium constants - all without any external input of energy.

We investigate the dynamics of both a single reaction and an ensemble of N identical reactions coupled to the cavity. In our single reactant studies, we find significant modification to the rate of reaction and to its quantum-mechanical equilibrium constant.

All of the effects observed in our single molecule studies are however found to diminish as the number of reactants is increased. For any experimentally relevant number of molecules, the cavity effects on the reaction rate and the equilibrium constant are therefore shown to be negligible within all theories considered in this thesis.

This thesis therefore does not offer any explanation for the experimental observations. It does however highlight issues with all current theoretical work on this topic, and provides suggestions - in light of the results presented here and in recent literature - as to what might be required to explain these effects.

Contents

List of Figures	ix
List of Abbreviations	xi
1 Introduction	1
2 Rate Theory	5
2.1 Classical Rate Theory	6
2.2 Ring Polymer Molecular Dynamics (RPMD)	8
2.2.1 Zero-Point Energy and Tunneling	11
2.3 RPMD Rate Theory	12
2.4 System–Bath Model	14
2.5 Transition State Theory (TST)	15
2.5.1 Harmonic Transition State Theory (HTST)	16
2.6 Kramer’s Theory	17
3 A Single Reaction in a Cavity	21
3.1 Reaction Rates for a Symmetric Double Well	21
3.2 The Pauli–Fierz Hamiltonian	24
3.3 Polariton Resonance	25
3.3.1 The Low Friction Regime	26
3.3.2 The High Friction Regime	29
3.3.3 Recrossing Effects on Reaction Rates	30
3.4 Conclusions	31
4 Collective Effects on Reaction Rates	33
4.1 Generalisation to N Reactants	33
4.2 Transition State Difficulties	34
4.3 Direct Simulation of N Reactants	36
4.3.1 The Model	38
4.3.2 Polariton Resonance in the Collective Regime	39
4.4 Conclusions	41

5	Cavity Effects on Equilibrium Constants	43
5.1	Single-Molecule Effects	44
5.2	N -Molecule Effects	47
5.3	Simulation	51
6	Conclusion	55
	Bibliography	59
	Appendices	
A	The Cayley Propagator	63
A.1	Cayley Propagator	63
B	Bath Discretisation and GLEs	69
B.1	Discrete Ohmic Baths	69
B.2	Discrete Debye baths	70
B.3	Generalised Langevin Equations (GLEs)	70
C	Model Parameters	71
C.1	Convergence information: Flux-Side Correlation	71
C.2	Convergence information: Direct Simulation	72
D	Outside-cavity Equilibria	73

List of Figures

1.1	An optical cavity	1
1.2	Experimental observations of resonance and the collective effect . .	3
2.1	Possible trajectory-based contributions to the flux–side correlation function	7
2.2	The ring polymer approximation to a quantum Hamiltonian	10
2.3	RPMD captures zero-point energy and tunneling	12
2.4	Rate-limiting factors in high and low friction regimes	18
2.5	A general example of Kramer’s turnover	19
3.1	The possible flow of energy for an open quantum system outside of a cavity	23
3.2	Kramer’s turnover for a single molecule outside of an optical cavity	23
3.3	The possible flow of energy for an isolated quantum system comprised of an optical cavity coupled to a molecule	25
3.4	The possible flow of energy for an open quantum system comprised of an imperfect optical cavity coupled to a single molecule	26
3.5	Cavity induced changes in rate in the low friction regime.	27
3.6	Cavity induced changes in rate in the high friction regime	30
3.7	Friction dependence of the transmission coefficient κ in classical dynamics and RPMD	31
4.1	The possible flow of energy for an open quantum system comprised of N molecules inside of a lossy optical cavity	34
4.2	‘Collective excitation’ requires N times larger activation energy and gives incorrect saddle-point index for ‘transition state’	35
4.3	Fitting procedure for direct simulation	37
4.4	Collective polariton resonance in low-friction regime	40
5.1	Equilibrium system setup	52
5.2	Equilibrium properties parameter scan	53
5.3	Equilibrium effects in the collective regime	54

List of Abbreviations

VSC	Vibrational strong coupling
PTA	1-phenyl-2-trimethylsilylacetylene
IR	Infrared
HTST	Harmonic transition state theory
TST	Transition state theory
RPMD	Ring polymer molecular dynamics
MD	Molecular dynamics
ZPE	Zero-point energy
QUAPI	Quasi-adiabatic propagator path integral
HEOM	Hierarchical equations of motion
GST	Ground-state tunneling
GLE	Generalised Langevin equations

1

Introduction

Synthetic chemists have long sought after ways to improve the selectivity and yield of their chemical transformations. Recently, a new method has emerged promising to achieve both of these features by selectively coupling vibrational modes of reactive systems to the vacuum state of light. This is known as chemistry under vibrational strong coupling (VSC).

When two highly reflective parallel mirrors are placed within micrometers of each other (shown in the left panel of Fig 1.1), photons - created by thermal quantum fluctuations of the vacuum field - resonate within them, forming standing

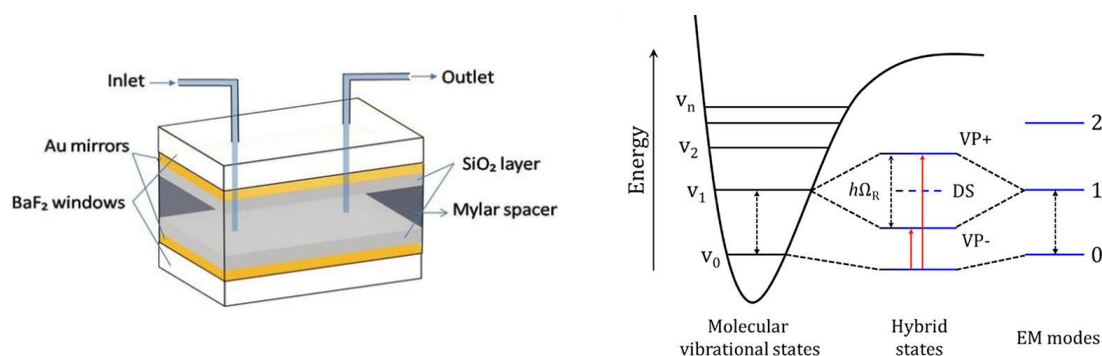


Figure 1.1: Left panel: The experimental setup for a chemical reaction occurring inside of a Fabry–Pérot optical cavity, adapted from Ref. [1]. Right panel: Coupling between molecular vibrations and cavity modes forms hybrid light-matter states known as the upper and lower vibrational polaritons (VP+ / VP-) adapted from Ref. [2] (right).

waves in the enclosed electromagnetic field. These standing waves are known as **cavity modes**, and have frequencies determined simply by the spacing between said mirrors. For the m^{th} cavity mode, the frequency of the wave in the direction perpendicular to the mirrors of spacing L_c is

$$\omega_{c,m} = \frac{mc\pi}{nL_c}, \quad (1.1)$$

where n is the refractive index of the cavity and c the speed of light [3]. If inside of this optical cavity there exist dipole-active molecular vibrational transitions of frequency close to $\omega_{c,m}$, they hybridise with the cavity mode, forming hybrid light-matter states known as **vibrational polaritons** (see right panel of Fig. 1.1). This combination is analogous to that observed in molecular orbital theory, such that the symmetric linear combination between photonic and vibrational states is stabilised relative to the unmixed states, and antisymmetric destabilised. These are known as the upper and lower polariton respectively.

The presence of these hybrid states is directly observable in the splitting of vibrational transition peaks in a cavity dipole absorption spectrum. The strength of interaction is quantified by the Rabi splitting observed for these peaks. When the cavity is resonant with an ensemble of N vibrational transitions, this splitting is

$$\Omega_R = 2\sqrt{N}g_0, \quad (1.2)$$

in which g_0 is the light-matter coupling strength, which will be further discussed in Sec 3.2.

It was first observed in 2012 [5] that performing certain chemical reactions inside of these optical cavities would significantly alter their rates. Since then, further experiments have found chemistry under vibrational strong coupling to influence chemoselectivity [6], equilibrium constants [7] and even stereoselectivity [8] of common chemical transformations. In addition, indirect modification of chemical reactivity

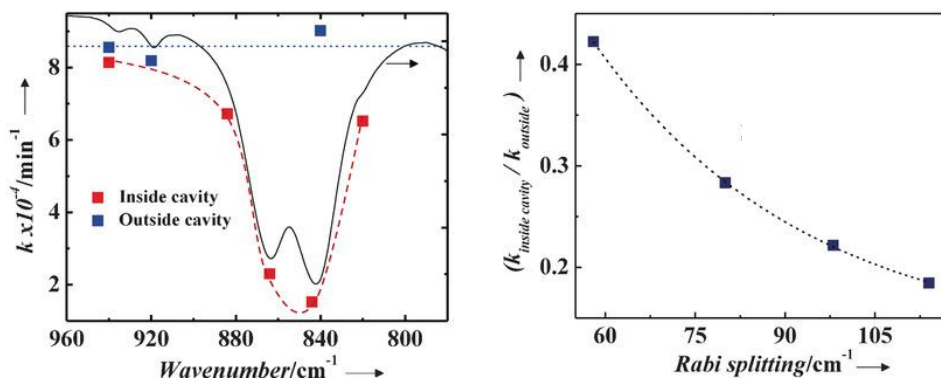


Figure 1.2: Cavity effects on the rate of the silane deprotection of 1-phenyl-2-trimethylsilylacetylene (PTA). Left panel: The rate is maximally suppressed by a **factor of 5.5** when a cavity mode is resonant with a reactant infrared (IR) transition (black line) - known as the ‘Resonance Effect’. Right panel: Cavity rate effects increase with Rabi splitting - known as the ‘Collective Effect’. Adapted from Ref. [4]

via solvent coupling has also been observed [1], extending possible applications to biological systems, in which cavity coupling has been used to modify enzyme activity in aqueous media [9, 10].

Fig 1.2 provides an example of this experimental evidence. In the left panel of Fig 1.2 the rate of the silane deprotection of 1-phenyl-2-trimethylsilylacetylene (PTA) is suppressed by more than 5 times - but only if the optical cavity is resonant with the reactant’s infrared active Si-C stretch (shown by the black line) - this is known as the **resonance effect**. The right panel of Fig 1.2 shows that as the Rabi splitting (which is proportional to \sqrt{N} , as in Eq. 1.2) is increased, the rate suppression of the deprotection reaction of PTA, when coupled to a resonant cavity mode is augmented. This is known as the **collective effect**.

There is significant desire in the scientific community for a theoretical explanation of these effects, as it would allow experimentalists to more effectively harness this new tool in their transformations. Despite this motivation however, there is so far no widely accepted theoretical explanation for any of these findings - which is relatively unsurprising considering the magnitude of the effects observed the fact that the process involves no external input of energy.

A common starting point is to consider a simplified model consisting of a single reaction vibrationally coupled to an optical cavity. In Ch. 3 I will look for the resonance effect in a double-well model, comparing a variety of rate theories (introduced in Ch. 2) for a condensed-phase reaction.

The experimental results found in the literature do not however refer to single reactions, but instead a large number (potentially as many as $\sim 10^{10}$) collectively coupled to the cavity. I will therefore in Ch. 4 extend the analysis to an ensemble of N reactants in order to understand cavity effects in the collective (experimentally relevant) regime. By explicitly simulating multiple reactive systems, I will examine the collective effect, as well as any changes in the resonance effect relative to the single molecule case.

In Ch. 5 I will then explore cavity effects on equilibrium constants, again looking for the resonance and collective effects. With these three approaches I hope to address all possible avenues by which chemical reaction dynamics may be modified by vibrational strong coupling, and perhaps provide some insight into the mechanism by which these effects operate.

2

Rate Theory

Contents

2.1	Classical Rate Theory	6
2.2	Ring Polymer Molecular Dynamics (RPMD)	8
2.2.1	Zero-Point Energy and Tunneling	11
2.3	RPMD Rate Theory	12
2.4	System–Bath Model	14
2.5	Transition State Theory (TST)	15
2.5.1	Harmonic Transition State Theory (HTST)	16
2.6	Kramer’s Theory	17

In this chapter, I will introduce theories by which the unimolecular rates of reaction for both quantum and classical systems will be calculated. Assume that the configuration space of a molecular system can be separated into reactants A and products B, with chemical equation



For a general non-equilibrium initial condition, there will be an initial transient behaviour,[11] which eventually settles to the kinetic equation such that

$$\dot{P}_A(t) = -k_f P_A(t) + k_b P_B(t) \quad (2.2)$$

and

$$\dot{P}_B(t) = k_f P_A(t) - k_b P_B(t), \quad (2.3)$$

in which $P_A(t)$ and $P_B(t)$ correspond to the population of A and B at time t respectively. The rate theories used yield k_f , the rate of forward reaction. At equilibrium, the ratio of forward to backward reactions is equal to the equilibrium constant, hence the rate of backward reaction k_b can easily be inferred. In this thesis the potential surfaces used when discussing polariton effects on reaction rates will be symmetric with respect to the reaction coordinate, hence $k_f = k_b = k$.

2.1 Classical Rate Theory

The thermal rate constant for a reaction on a 1-dimensional potential energy surface can be expressed as,

$$k(T) = \frac{1}{Q_r} \lim_{t \rightarrow t_p} c_{fs}(t), \quad (2.4)$$

where Q_r is the reactant partition function (per unit volume for reactions in three dimensions) [12]. The dividing surface is defined as $q = q^\ddagger$. Here $c_{fs}(t)$ is the correlation function between flux of reactants through the dividing surface at time 0 and the population on the product side of this surface at t . The ‘plateau time’ of c_{fs} , t_p is long enough such that the initial transient behaviour of the reactive system is removed from the calculation of rate. The classical limit of c_{fs} is

$$c_{fs}^{cl}(t) = \frac{1}{2\pi\hbar} \int dp_0 \int dq_0 e^{-\beta H(p_0, q_0)} \dot{\theta}(q_0 - q^\ddagger) \theta(q_t - q^\ddagger). \quad (2.5)$$

where q_0 and q_t correspond to the reaction coordinate at time 0 and t respectively. This notation is also used for p , the momentum. The classical side operator, $\theta(q - q^\ddagger)$ is a Heaviside step function. The classical flux operator is its time derivative;

$$\dot{\theta}(q_0 - q^\ddagger) = \frac{dq_0}{dt} \delta(q_0 - q^\ddagger) = \frac{p_0}{m} \delta(q_0 - q^\ddagger). \quad (2.6)$$

The integral in Eq. (2.5) can therefore be seen as a sum going over only trajectories starting at the transition state, where $q_0 = q^\ddagger$ - such that $\delta(q_0 - q^\ddagger) \neq 0$. Each trajectory is weighted by its Boltzmann factor $e^{-\beta H(p_0, q_0)}$ and initial velocity $\frac{p_0}{m}$ - a weighting that therefore is positive if the trajectory's initial velocity is from reactants to products or negative if in the opposite direction. At time t , all trajectories with $q_t \geq q^\ddagger$ will have a non-zero θ and will hence contribute their weight to the value of $c_{\text{fs}}(t)$.

If a given trajectory crosses the dividing surface at $t > 0$ it is considered to have 'recrossed' the dividing surface. The effect of recrossing on $c_{\text{fs}}(t)$ can be understood by considering two types of trajectory after some small time ϵ (before recrossing);

- i) $p_0 > 0 \implies q_\epsilon > q^\ddagger \quad \therefore \quad \frac{p_0}{m} \theta(q_\epsilon - q^\ddagger) > 0$ [positive contribution to $c_{\text{fs}}(\epsilon)$]
- ii) $p_0 < 0 \implies q_\epsilon < q^\ddagger \quad \therefore \quad \frac{p_0}{m} \theta(q_\epsilon - q^\ddagger) = 0$ [no contribution to $c_{\text{fs}}(\epsilon)$]

Now consider these scenarios at time t , after which recrossing - or any odd number of recrossings - has already occurred;

- i) $q_t > q^\ddagger \quad \therefore \quad \frac{p_0}{m} \theta(q_t - q^\ddagger) = 0$ [no contribution to $c_{\text{fs}}(t)$]
- ii) $q_t > q^\ddagger \quad \therefore \quad \frac{p_0}{m} \theta(q_t - q^\ddagger) < 0$ [negative contribution to $c_{\text{fs}}(t)$]

The result of recrossing is therefore either : i) - removal of a positive contribution or ii) - introduction of a negative contribution to $c_{\text{fs}}(t)$. Hence as both types contribute negatively, $c_{\text{fs}}^{\text{cl}}$ is a decreasing function in time.

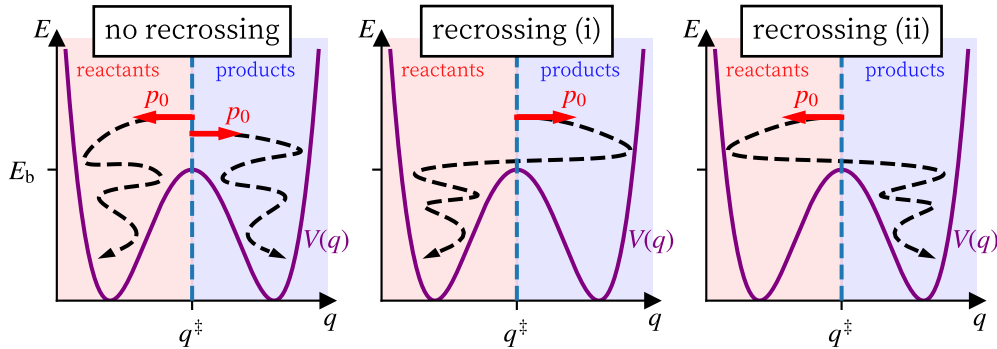


Figure 2.1: A diagram showing possible trajectories' contributions to c_{fs}

The full rate of reaction, including recrossing effects is therefore given by the plateau value of Eq. (2.4).

2.2 Ring Polymer Molecular Dynamics (RPMD)

Quantum rates of reaction could of course be obtained by substituting the quantum-mechanical flux-side correlation function, $c_{\text{fs}}^{\text{qm}}(t)$ into Eq. (2.4). In general - and especially in the condensed phase - simulation of this unfortunately would be prohibitively computationally expensive. Ring polymer molecular dynamics is a relatively inexpensive semi-classical method which offers a very good approximation to the quantum rate by using Feynman path integrals. In this section I will outline a simple derivation of the path integral form of a partition function [13], then explain how this can be extended such that it can apply to rate theory [14].

In this derivation, integrals are over all space unless otherwise specified. The momenta and position coordinates, p and q are 1-dimensional here, but multidimensional generalisation is straightforward (adding an index to each). The assumed information is as follows [15];

$$\begin{aligned} \text{tr} [\hat{O}] &\equiv \int dq \langle q | \hat{O} | q \rangle & \langle q | p \rangle &= \sqrt{\frac{1}{2\pi\hbar}} e^{ipq/\hbar} \\ \hat{1} &= \int dp |p\rangle \langle p| & \hat{1} &= \int dq |q\rangle \langle q|. \end{aligned}$$

The partition function of a system is the trace of the Boltzmann operator,

$$Q = \text{tr} [e^{-\beta\hat{H}}] \equiv \int dq \langle q | e^{-\beta\hat{H}} | q \rangle. \quad (2.7)$$

Let us factorise Eq. (2.7) into n terms as such,

$$Q = \int dq \langle q | (e^{-\beta_n\hat{H}}) (e^{-\beta_n\hat{H}}) \dots | q \rangle, \quad (2.8)$$

where $\beta_n = \frac{\beta}{n} \equiv \frac{1}{nk_{\text{B}}T}$, for which n is a positive integer. Now, let us insert the identity in between each exponential ($n - 1$ times). Each identity corresponds to integration

over a different dummy variable, of which we will denote dq_1 (corresponding to the first dq in the trace above) $dq_2\dots dq_n$.

$$Q = \int dq_1\dots dq_n \langle q_1 | e^{-\beta_n \hat{H}} | q_2 \rangle \langle q_2 | e^{-\beta_n \hat{H}} | q_3 \rangle \dots \langle q_n | e^{-\beta_n \hat{H}} | q_1 \rangle. \quad (2.9)$$

This integral now consists of n factors of the form $\langle q_j | \hat{O} | q_{j+1} \rangle$, with a cyclic index such that $q_{n+1} \equiv q_1$. Looking at each one of these terms, by considering the second order Taylor expansion of $e^{-\beta_n \hat{H}} = e^{-\beta_n (\hat{T} + \hat{V})}$ we get

$$\langle q_j | e^{-\beta_n \hat{H}} | q_{j+1} \rangle \simeq \langle q_j | e^{-\frac{\beta_n \hat{V}}{2}} e^{-\beta_n \hat{T}} e^{-\frac{\beta_n \hat{V}}{2}} | q_{j+1} \rangle + O(1/n^3). \quad (2.10)$$

The potential energies can now be evaluated, on ‘either side’ (as \hat{V} is hermitian),

$$\langle q_j | e^{-\frac{\beta_n \hat{V}}{2}} e^{-\beta_n \hat{T}} e^{-\frac{\beta_n \hat{V}}{2}} | q_{j+1} \rangle = e^{-\frac{\beta_n V(q_j)}{2}} \langle q_j | e^{-\beta_n \hat{T}} | q_{j+1} \rangle e^{-\frac{\beta_n V(q_{j+1})}{2}}. \quad (2.11)$$

Next, to evaluate $e^{-\beta_n \hat{T}}$ we insert the identity in the momentum eigenbasis,

$$\begin{aligned} \langle q_j | e^{-\frac{\beta_n \hat{V}}{2}} e^{-\beta_n \hat{T}} e^{-\frac{\beta_n \hat{V}}{2}} | q_{j+1} \rangle = \\ \int dp e^{-\frac{\beta_n V(q_j)}{2}} \langle q_j | p \rangle e^{-\frac{\beta_n p^2}{2m}} \langle p | q_{j+1} \rangle e^{-\frac{\beta_n V(q_{j+1})}{2}}. \end{aligned} \quad (2.12)$$

Inserting $\langle q_j | p \rangle$ and $\langle p | q_{j+1} \rangle$ and integration over dp gives,

$$\begin{aligned} \langle q_j | e^{-\frac{\beta_n \hat{V}}{2}} e^{-\beta_n \hat{T}} e^{-\frac{\beta_n \hat{V}}{2}} | q_{j+1} \rangle = \int dp e^{-\frac{\beta_n (V(q_j) + V(q_{j+1}))}{2}} e^{-\frac{\beta_n p^2}{2m} - \frac{-ip(q_j - q_{j+1})}{\hbar}} \\ = \frac{1}{2\pi\hbar} \sqrt{\frac{2\pi m}{\beta_n}} e^{-\beta_n \left[\frac{m\omega_n^2 (q_j - q_{j+1})^2}{2} + \frac{V(q_j)}{2} + \frac{V(q_{j+1})}{2} \right]}, \end{aligned} \quad (2.13)$$

where we have defined $\omega_n = \frac{1}{\beta_n \hbar}$. We can now re-introduce the integral over momenta. This is the key step that allows sampling of system using molecular dynamics (MD). Therefore,

$$\langle q_j | e^{-\beta_n \hat{H}} | q_{j+1} \rangle = \frac{1}{2\pi\hbar} \int dp e^{-\beta_n \left[\frac{p^2}{2m} + \frac{m\omega_n^2 (q_j - q_{j+1})^2}{2} + \frac{V(q_j)}{2} + \frac{V(q_{j+1})}{2} \right]} + O(1/n^3). \quad (2.14)$$

This can now be re-inserted into Eq. (2.9) with each integral over dp getting its own index in the same way as $dq_1\dots dq_n$. Let us compact this notation such that

$dq_1 \dots dq_n \equiv \mathbf{dq}$, and analogously for momenta. Note that the overall error is now of order $1/n^2$ as the approximation of Eq. (2.10) is made n times [16].

$$\begin{aligned}
Q &= \left(\frac{1}{2\pi\hbar} \right)^n \int \mathbf{dp} \int \mathbf{dq} \prod_{j=1}^n e^{-\beta_n \left[\frac{p_j^2}{2m} + \frac{m\omega_n^2(q_j - q_{j+1})^2}{2} + \frac{V(q_j)}{2} + \frac{V(q_{j+1})}{2} \right]} + O(1/n^2) \\
&\equiv \left(\frac{1}{2\pi\hbar} \right)^n \int \mathbf{dp} \int \mathbf{dq} e^{-\beta_n \sum_{j=1}^n \left[\frac{p_j^2}{2m} + V(q_j) + \frac{m\omega_n^2(q_j - q_{j+1})^2}{2} \right]} + O(1/n^2).
\end{aligned} \tag{2.15}$$

By inspection of Eq. (2.15) one can see that the quantum partition function has been mapped that of a classical system in an extended phase space. This effective classical Hamiltonian is,

$$H_n(\mathbf{p}, \mathbf{q}) = \sum_{j=1}^n \left[\frac{p_j^2}{2m} + V(q_j) + \frac{1}{2} m\omega_n^2 (q_j - q_{j+1})^2 \right], \tag{2.16}$$

which is comprised of n copies of the system corresponding to the classical limit of the initial quantum Hamiltonian, $H_{cl}(p_j, q_j)$, with adjacent copies linked together by classical harmonic springs, as illustrated in Fig. 2.2. The phase-space variables \mathbf{p} and \mathbf{q} are now vectors containing p_j and q_j respectively. The index j corresponds to each 'bead' on the ring polymer necklace, with n giving the total number of beads.

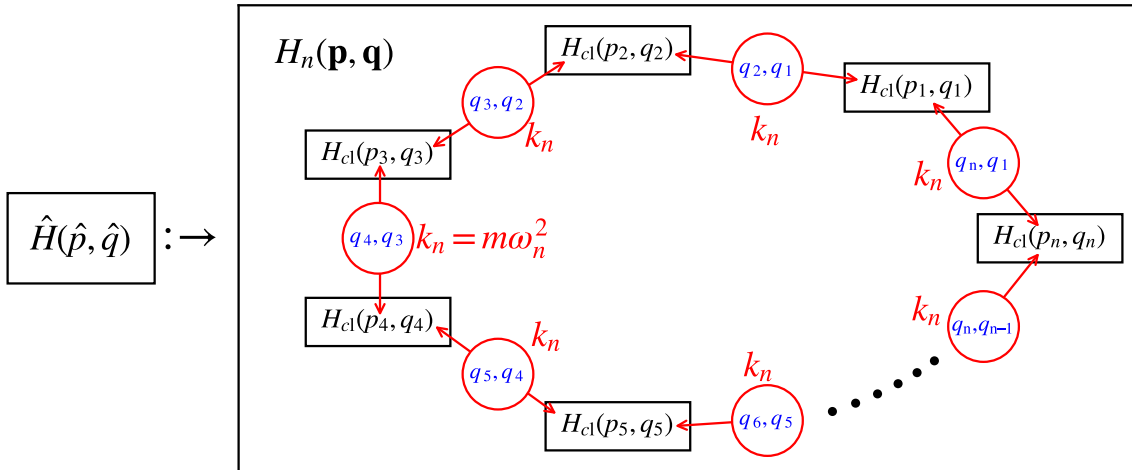


Figure 2.2: A diagram showing the ring polymer approximation to a quantum Hamiltonian. Blue text indicates which coordinates are linearly coupled together (i.e. coupling via harmonic springs with spring constant k_n). Red text indicates possible energy transfer pathways between beads (via said springs).

As $n \rightarrow \infty$, the error will tend to zero, but for most systems of interest at ambient

temperatures [17] we find sufficient convergence with $n = 32$ as this value makes $\frac{\beta\hbar\omega_{\max}}{n} \gg 1$, where ω_{\max} is the max frequency of said systems.

2.2.1 Zero-Point Energy and Tunneling

RPMD goes beyond classical MD and includes quantum statistical effects such as zero-point energy (ZPE) and quantum tunneling. These effects can be very important in condensed phase reactions - in particular for systems including light atoms such as Hydrogen. At high temperature, the ring polymer springs become stiff and as such, the ring polymer shrinks to a classical particle. At low temperature however, the ring polymer 'swells' such that the bead distribution recovers the probability distribution of the quantum wave function. The swelling is about the **centroid**, the classical 'position' of this quantum particle,

$$\bar{q} = \frac{1}{n} \sum_{j=1}^n q_j. \quad (2.17)$$

The thermally averaged radius of gyration of a free n bead ring polymer is [17]

$$\Delta q_n = \sqrt{\frac{\beta\hbar^2}{12m} \left(1 - \frac{1}{n^2}\right)}. \quad (2.18)$$

Note that swelling persists as $n \rightarrow \infty$, and can be seen as a consequence of the Heisenberg uncertainty principle.

With this in mind, the potential experienced by the centroid relative to the potential averaged over the beads at some finite temperature can be calculated. In a potential well (left panel of Fig. 2.3) the potential averaged over beads is greater than that of the centroid. In this case, zero-point energy (ZPE) is added to the classical potential. When the ring polymer is passing over a barrier (right panel of Fig. 2.3) however, the average potential experienced by the beads is smaller than that of the centroid. This implies that barrier crossing may occur even when the system energy is less than that of the classical barrier height, hence facilitating quantum tunneling through said barrier.

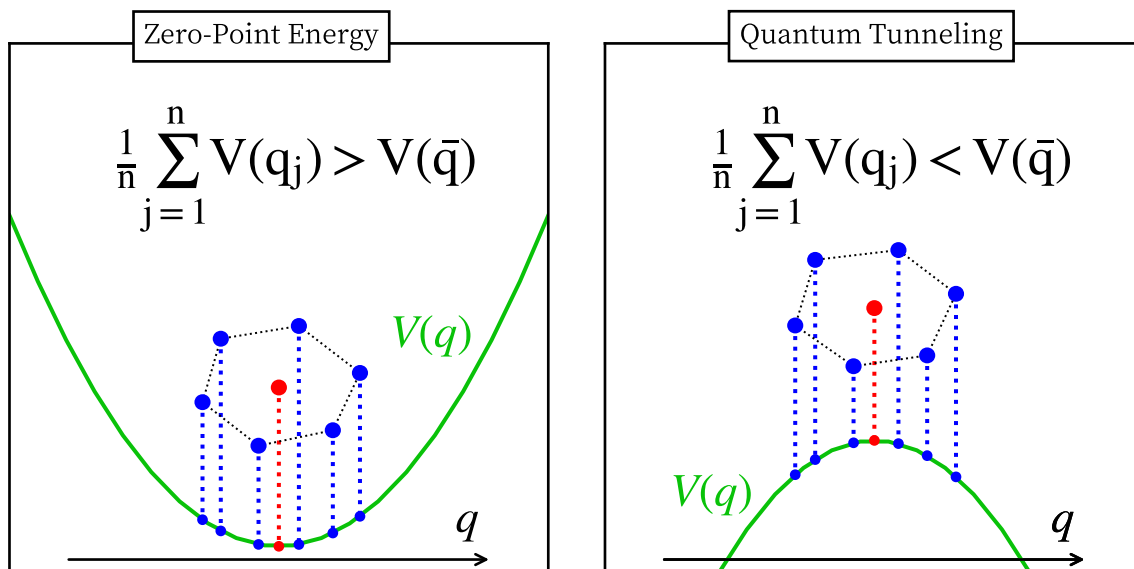


Figure 2.3: A diagram showing how the swelling of a ring polymer confined to a potential well (left) and passing over a potential barrier (right) captures zero-point energy and tunneling. Red dots annotate the centroid, and blue the ring polymer beads.

Its derivation proves that RPMD will capture the exact quantum statistics of a system. It does not prove that real-time system dynamics are exact, and since it does not involve any phases that **RPMD cannot capture real-time quantum coherences**. The dynamics produced do conserve the Boltzmann distribution making RPMD nonetheless an effective method for approximating quantum correlation functions [18]. In addition, for reactions occurring in the condensed phase at room temperature, quantum decoherence is rapid - heavily reducing the coherences - making RPMD well suited for simulation of chemical reaction dynamics.

2.3 RPMD Rate Theory

As RPMD is simply classical mechanics in an extended phase-space [16], one can define a function analogous to the classical flux-side correlation and use this to define a reaction rate.

$$c_{\text{fs}}^{\text{RPMD}}(t) = \left(\frac{1}{2\pi\hbar} \right)^n \int \mathbf{d}\mathbf{p}_0 \int \mathbf{d}\mathbf{q}_0 e^{-\beta_n H_n(\mathbf{p}_0, \mathbf{q}_0)} \dot{\theta}(s(\mathbf{q}_0)) \theta(s(\mathbf{q}_t)). \quad (2.19)$$

The dividing surface between reactants and products is defined at $s(\mathbf{q}) = 0$. It can be shown [19] that the rate of reaction is independent of the choice of $s(\mathbf{q})$. A simple choice (which we will use in this thesis) is to use the centroid - as defined in Eq. (2.17) - of the ring polymer to define the dividing surface, such that

$$s(\mathbf{q}) = \frac{1}{n} \sum_{j=1}^n (q_j) - q^\ddagger. \quad (2.20)$$

The resulting flux operator $\dot{\theta}(s(\mathbf{q}))$ is obtained by taking the time derivative of $\theta(s(\mathbf{q}))$ with the help of the chain rule,

$$\begin{aligned} \dot{\theta}(s(\mathbf{q})) &= \delta(s(\mathbf{q})) \sum_{j=1}^n \left[\frac{\partial s(\mathbf{q})}{\partial q_j} \frac{dq_j}{dt} \right] \\ &= \delta(\bar{q} - q^\ddagger) \frac{\bar{p}}{m}, \end{aligned} \quad (2.21)$$

where \bar{p} is the centroid momentum, defined analogously to \bar{q} . Lastly, $H_n(\mathbf{p}, \mathbf{q})$ is just as defined in Eq. (2.16) and is formed by ‘ring polymerising’ the classical limit of the quantum Hamiltonian.

With this framework now in place, RPMD can be used to generate trajectories with which this integral in Eq. (2.19) may be numerically evaluated. A set of initial phase points are generated, with the centroid fixed to the diving surface at $t = 0$. Then, trajectories are numerically integrated in time according to Hamilton’s equations:

$$\frac{dq_j}{dt} = \frac{\partial H_n}{\partial p_j}, \quad \frac{dp_j}{dt} = -\frac{\partial H_n}{\partial q_j}. \quad (2.22)$$

After each time step, $\theta(s(\mathbf{q}_t))$ measures if the trajectory is on the product side. The function $c_{\text{fs}}^{\text{RPMD}}(t)$ is calculated by averaging over many trajectories with associated weightings as mentioned in Sec. 2.1, until convergence. The single bead limit of RPMD reduces to classical rate theory, as for $n = 1$: $\bar{q} \equiv q$ and $H_n(\mathbf{p}, \mathbf{q}) \equiv H_{\text{cl}}(p, q)$, hence classical rates are obtained by the same method. Note that for increased stability in the integration of RPMD equations of motion we used the ‘Cayley propagator’ - details of which can be found in Appendix A.

2.4 System–Bath Model

The effect of a solvent is often a crucial component in the understanding of chemical reaction dynamics. The system–bath model is commonly used to simulate the effects of a solvent, treating its impact on the reaction dynamics as an effective friction. To model this friction we couple our reaction to a bath of harmonic oscillators.

$$\hat{H}(\hat{p}, \hat{q}, \hat{\mathbf{P}}, \hat{\mathbf{Q}}) = \hat{H}_{\text{sys}}(\hat{p}, \hat{q}) + \hat{H}_{\text{bath}}(\hat{\mathbf{P}}, \hat{\mathbf{Q}}, \hat{q}), \quad (2.23)$$

where \hat{H}_{sys} is the Hamiltonian of the isolated quantum system and

$$\hat{H}_{\text{bath}}(\hat{\mathbf{P}}, \hat{\mathbf{Q}}, \hat{q}) = \sum_{i=1}^{n_{\text{B}}} \left[\frac{\hat{P}_i^2}{2} + \frac{1}{2} \omega_{\text{Bi}}^2 \left(\hat{Q}_i + \frac{c_{\text{Bi}}}{\omega_{\text{Bi}}^2} \hat{q} \right)^2 \right]. \quad (2.24)$$

The ‘bath’ in question is simply n_{B} quantum harmonic oscillators (known as ‘bath modes’) each of natural frequency ω_{Bi} . Each oscillator is linearly coupled to the system’s reaction coordinate, \hat{q} , with coupling strength c_{Bi} , facilitating reversible energy exchange between system and bath. These parameters are selected from the spectral density function,

$$J(\omega) = \frac{\pi}{2} \sum_{i=1}^{n_{\text{B}}} \frac{c_{\text{Bi}}^2}{\omega_{\text{Bi}}} \delta(\omega - \omega_{\text{Bi}}), \quad (2.25)$$

which contains all information about the bath and its coupling to the system. The spectral density is often modelled as a linear function at small ω multiplied by a cutoff function at large ω . In this thesis we will use the Ohmic,

$$J_{\text{Ohm.}}(\omega) = \eta_{\text{B}} \omega e^{-\omega/\gamma_{\text{B}}}, \quad (2.26)$$

and the Debye,

$$J_{\text{Deb.}}(\omega) = \eta_{\text{B}} \omega \frac{\gamma_{\text{B}}^2}{\omega^2 + \gamma_{\text{B}}^2} \quad (2.27)$$

spectral densities, for both of which η_{B} controls the magnitude of friction and γ_{B} the shape of $J(\omega)$ of bath ‘B’.

To allow an explicit simulation only a finite number of bath ‘modes’ - a harmonic oscillator of frequency ω_{B_i} coupled with coupling c_{B_i} - are employed. Details of this discretisation and the parameters used can be found in Appendices B and C respectively.

The notation used above will be continued throughout this thesis, with capitalised coordinates being used for the bath coupled to an un-capitalised coordinate just as the bath coordinates \hat{Q}_i are coupled to the system coordinate \hat{q} in Eq. (2.24).

2.5 Transition State Theory (TST)

The Eyring equation [20] is a common tool used by the undergraduate chemist to obtain the Transition State Theory (TST) rate of reaction. For a uni-molecular reaction,

$$k^{\text{TST}}(T) = \frac{1}{\beta h} \frac{Q_{\ddagger}}{Q_r} e^{-\beta E_b}, \quad (2.28)$$

where Q_r and Q_{\ddagger} correspond to the reactant and transition state partition functions respectively, $\beta = \frac{1}{k_B T}$ where T is the temperature and k_B the Boltzmann constant. As usual, Q_{\ddagger} has a single vibrational degree of freedom removed, corresponding to movement over the barrier. Note that the zero-point energies of reactants and products are included within their partition functions, **not** E_b (which is the classical barrier height of the reaction).

It can be shown [19] that the transition state theory rate of reaction can be obtained from $c_{\text{fs}}^{\text{cl}}(t \rightarrow 0^+)$ as

$$k^{\text{TST}} = \frac{1}{Q_r} c_{\text{fs}}(t \rightarrow 0^+), \quad (2.29)$$

where c_{fs} is either the classical or ring polymer flux-side correlation function, to yield the classical or quantum transition state theory rates respectively.

2.5.1 Harmonic Transition State Theory (HTST)

A faster, but approximate, way of obtaining transition state theory rates is by making a harmonic approximation to the reactant and transition state partition functions.

Consider the partition function of a ‘ring polymerised’ harmonic oscillator. Its n -bead Hamiltonian is

$$H_n(\mathbf{p}, \mathbf{q}) = \sum_{j=1}^n \left[H_{\text{cl}}(p_j, q_j) + \frac{1}{2} m \omega_n^2 (q_j - q_{j+1})^2 \right], \quad (2.30)$$

where as usual $q_{n+1} \equiv q_1$ and

$$H_{\text{cl}}(p, q) = \frac{p^2}{2} + \frac{1}{2} \lambda^2 q^2 \quad (2.31)$$

is the Hamiltonian of a classical harmonic oscillator of natural frequency λ with unit mass. It can be shown [16] that the partition function of this system is

$$Q_n = \prod_{j=1}^n \left(4 \sin^2 \left(\frac{j\pi}{n} \right) + \left(\frac{\beta \hbar \lambda}{n} \right)^2 \right)^{1/2}. \quad (2.32)$$

As was shown in Sec. 2.2, the $n \rightarrow \infty$ limit of Eq. (2.32) will yield the exact partition function of a quantum harmonic oscillator. Evaluation of said limit was found in the appendix of [16].

$$Q_{\text{qm}} = \lim_{n \rightarrow \infty} [Q_n] = \frac{1}{2 \sinh(\beta \hbar \lambda / 2)}. \quad (2.33)$$

This reduces to the classical partition function,

$$Q_{\text{cl}} \equiv Q_{n=1} = \frac{1}{\beta \hbar \lambda}, \quad (2.34)$$

when $\beta \hbar \lambda \ll 1$ so the high temperature ($\beta \rightarrow 0$) limit of Eq. (2.33) recovers the classical result in Eq. (2.34), as expected.

By taking a second order Taylor expansion of $V(q)$, the potential energy surface along the reaction coordinate at either the reactants ($q = q_r$) or transition state ($q = q^\ddagger$) stationary point, a local harmonic approximation of the Hamiltonian can be made;

$$V_{\text{rct}}(q) \simeq \frac{1}{2} m \omega_r^2 (q - q_r)^2 \quad \text{and} \quad V_{\ddagger}(q) \simeq E_b - \frac{1}{2} m \omega_b^2 (q - q^\ddagger)^2. \quad (2.35)$$

With this expansion in place, all terms in the total classical Hamiltonian - even when including a dissipative bath - are of maximum order harmonic. This means that by taking normal modes - via diagonalisation of the mass-weighted Hessian, the Hamiltonian can be expressed as a sum of uncoupled harmonic oscillators, each with natural frequency λ_i .

The transition state Hamiltonian will have one imaginary frequency: $i\lambda_{\ddagger}$. This frequency is discarded as it corresponds to movement over the reaction barrier; an inverted potential. The reactant and transition state partition functions, Q_r and Q_{\ddagger} can then be constructed as a product of the partition functions for each normal mode either classical or quantum - and inserted into Eq. (2.28). Therefore the classical rate constant is

$$k_{\text{cl}}^{\text{HTST}} = \frac{1}{2\pi} e^{-\beta E_b} \prod_i^{\ddagger} \frac{1}{\lambda_i} \prod_j^r \lambda_j . \quad (2.36)$$

Its quantum counterpart is

$$k_{\text{qm}}^{\text{HTST}} = \frac{2}{\beta h} e^{-\beta E_b} \prod_i^{\ddagger} \frac{1}{\sinh(\beta \hbar \lambda_i / 2)} \prod_j^r \sinh(\beta \hbar \lambda_j / 2) , \quad (2.37)$$

which now includes the contribution of zero-point energy to reaction rate, but will **not** include quantum tunneling through the barrier, as this degree of freedom was removed.

2.6 Kramer's Theory

For both the classical and quantum rates, there exists a value of solvent friction at which the rate of reaction is maximised. This is known as **Kramer's Turnover** [21] and be explained in terms of the trajectory-based interpretation of c_{fs} as laid out in Sec. 2.1, recalling that recrossing of the dividing surface of a trajectory strictly leads to a decrease in c_{fs} .

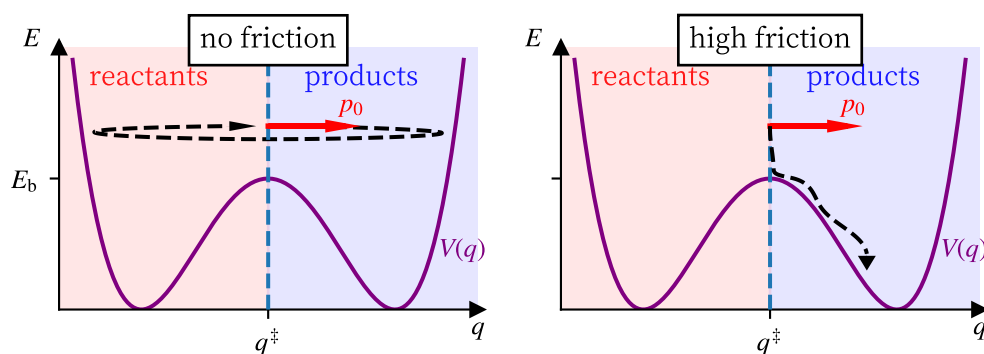


Figure 2.4: Rate-limiting factors in high and low friction regimes

For the limit of no solvent friction, no energy is dissipated into the surroundings. This means that all trajectories starting at the dividing surface cross from reactant to products, then recross to re-form reactants etc. As a consequence, the overall rate of reaction is zero, as there is no net flow from reactants to products (see left panel of Fig. 2.4). As solvent friction is increased, the amount of recrossing decreases, thus increasing the rate of reaction. At the limit of high friction however there is no recrossing at all. The rate is instead decreased at high friction due to an increasingly small Boltzmann weighting (see Sec. 2.1) being given to each trajectory. This effect is observed because the additional bath Hamiltonian (see Sec. 2.4) is of course included in the total Hamiltonian by which this weighting is calculated. Kramer's theory simply combines these limits giving a maximum in rate at some intermediate friction. This is known as 'Kramer's Turnover'.

With the aforementioned models in place, they can be tested against some exact quantum (Quasi-Adiabatic propagator Path Integral; QUAPI) and classical data [22] for a general double-well transition problem, shown in Fig. 2.5. Full details of the model are given in Ref. [22]. Note that the vertical axis is the dimensionless ratio between k , the rate of reaction and k_0 , the rate of classical transition state theory rate for $\eta_s = 0$. As transition state theory does not take into account recrossing of the dividing surface, it is not appropriate to calculate rates in the low-friction limit. After turnover however, it reproduces the exact results very well. Quantum Harmonic

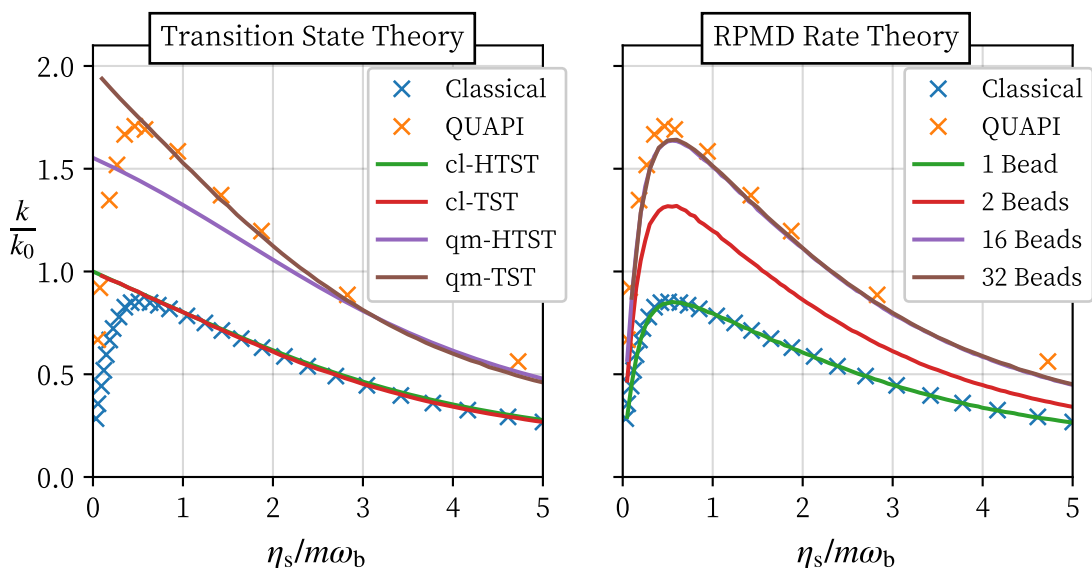


Figure 2.5: Reaction rate dependence on solvent friction for the system of [22], normalised by k_0 the classical TST rate corresponding to $\eta_s = 0$. The dimensionless ratio $\eta_s/m\omega_b$ measures the strength of the solvent friction relative to reactant mass \times barrier frequency (a constant).

Transition State Theory (qm-HTST) does not take into account tunneling through the barrier, and hence under-estimates the rate of reaction. Any discrepancy between classical Harmonic Transition State Theory (cl-HTST) and classical Transition State Theory (cl-TST) can be attributed to the anharmonicity of the barrier, but as can be seen it is very minor.

The effect of recrossing can be taken into account with RPMD (right panel) with 1 and 32 beads almost quantitatively capturing the entire rate profile from low to high friction for classical and quantum rates respectively. As these methods are trajectory-based, there are errors in calculation that can be attributed to lack of convergence in: the length and number of trajectories, the number of bath modes on each bath, the number of ring polymer beads (for the quantum case) etc. For the rest of this thesis, 32 beads will be used for quantum RPMD simulations - which was found to give converged results in all cases. The details about other convergence parameters can be found in Appendix C.

3

A Single Reaction in a Cavity

Contents

3.1	Reaction Rates for a Symmetric Double Well	21
3.2	The Pauli–Fierz Hamiltonian	24
3.3	Polariton Resonance	25
3.3.1	The Low Friction Regime	26
3.3.2	The High Friction Regime	29
3.3.3	Recrossing Effects on Reaction Rates	30
3.4	Conclusions	31

3.1 Reaction Rates for a Symmetric Double Well

In a recent paper [23] Lindoy *et al.* used Hierarchical Equations of Motion (HEOM), a numerically exact quantum method, to simulate reaction rates in a double-well potential. For a molecular system undergoing some generic reaction in a double-quartic potential well, the Hamiltonian is

$$\hat{H}_{\text{mol}} = \hat{T}_{\text{mol}}(\hat{p}) + \hat{V}_{\text{mol}}(\hat{q}), \quad (3.1)$$

in which

$$\hat{T}_{\text{mol}} = \frac{\hat{p}^2}{2} \quad \text{and} \quad \hat{V}_{\text{mol}} = \frac{\omega_{\text{b}}^4}{16E_{\text{b}}}\hat{q}^4 - \frac{\omega_{\text{b}}^2}{2}\hat{q}^2. \quad (3.2)$$

The parameters ω_b and E_b give the classical barrier frequency and height relative to the bottom of the reactant well respectively. The reaction coordinate \hat{q} is parametrically dependent on the molecular system’s Cartesian coordinates, and \hat{p} is the conjugate momentum. Note that we use mass-scaled coordinates throughout this thesis

Lindoy *et al.* explored several parameter regimes some of which had a significant ground-state tunneling (GST) contribution to reaction rate. As this effect is untypical for reactions occurring in the condensed phase, the main focus in this thesis will be on a symmetric double well with $\omega_b = 500 \text{ cm}^{-1}$ and $E_b = 2000 \text{ cm}^{-1}$, for which the GST contribution to rate is negligible in comparison to the total rate. For this double well, the reactant harmonic frequency is $\omega_r = \sqrt{2} \omega_b = 707 \text{ cm}^{-1}$. The temperature for the simulations was set to 300 K.

To simulate the effect of solvent friction, the system–bath model can be used. Hence, for a single reactant in an open system,

$$\hat{H}_{\text{tot}} = \hat{H}_{\text{mol}}(\hat{p}, \hat{q}) + \hat{H}_{\text{solv}}(\hat{\mathbf{P}}, \hat{\mathbf{Q}}, \hat{q}), \quad (3.3)$$

where

$$\hat{H}_{\text{solv}} = \sum_{i=1}^{n_S} \left[\frac{\hat{P}_i^2}{2} + \frac{1}{2} \omega_{S_i}^2 \left(\hat{Q}_i + \frac{c_{S_i}}{\omega_{S_i}^2} \hat{q} \right)^2 \right]. \quad (3.4)$$

The parameter η_s is used to control the strength of coupling between the reaction coordinate and its environment (the solvent) as discussed in Sec. 2.4. The values of discretised bath frequencies and coupling constants, $\{c_{S_i}\}$ and $\{\omega_{S_i}\}$, are obtained from the solvent spectral density $J_S(\omega)$ and η_s respectively as explained in Appendix B.

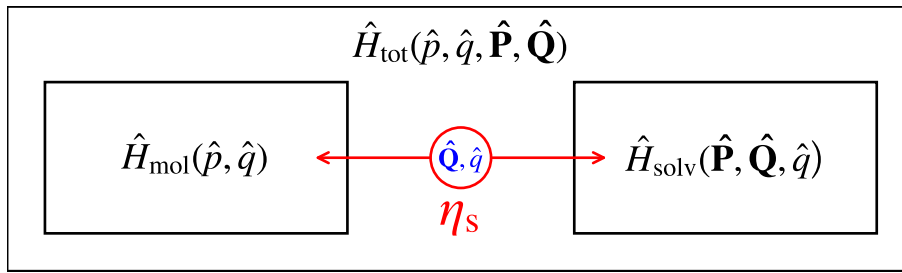


Figure 3.1: A diagram to show the possible flow of energy for an open quantum system outside of a cavity. The red arrow indicates the flow of energy between sub-systems, blue text indicates which coordinates are linearly coupled together.

First, we consider the reaction rate outside a cavity. The HEOM outside-cavity Kramer’s Turnover behaviour is compared with that of the rate theories introduced in Ch. 2 for this model in Fig. 3.2.

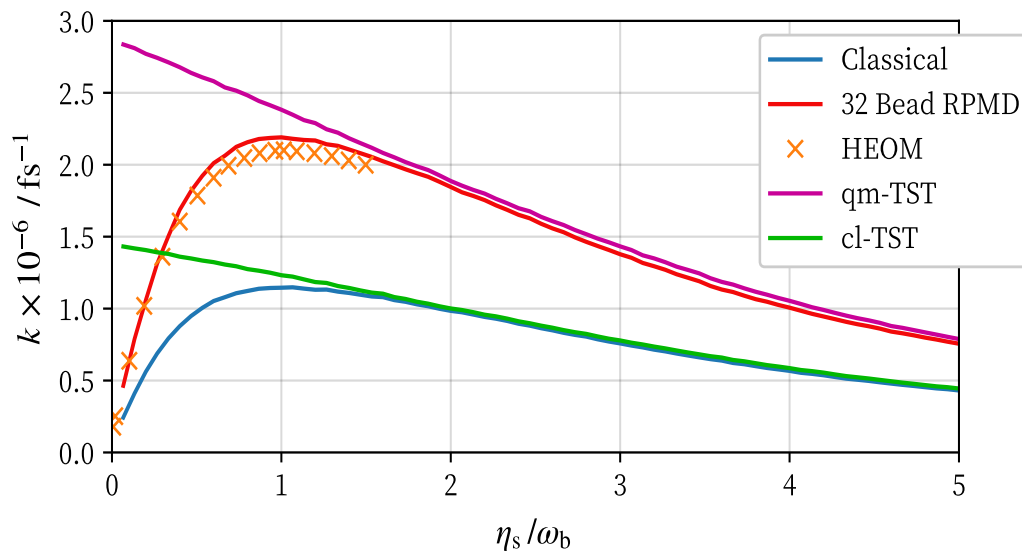


Figure 3.2: Kramer’s turnover for a single molecule outside of an optical cavity. The dimensionless ratio η_s / ω_b is between the solvent friction strength and barrier frequency (a constant)

Classical rate theory does not include the effects of zero-point energy or quantum tunneling, both of which augment the reaction rate. For this reason, it underestimates the rate of reaction by roughly a factor of 2. In contrast, RPMD rate theory includes these effects and can be seen to almost quantitatively capture the exact quantum Kramer’s Turnover for this system. By comparing to transition state theory, the effects of recrossing on the reaction rate can be seen to be significant for low friction

and small for high friction, as expected from the discussion in Sec. 2.6.

3.2 The Pauli–Fierz Hamiltonian

The Pauli–Fierz (PF) Hamiltonian is used to describe interactions between light and matter. Assumptions in its derivation involve the long wavelength approximation (assuming the cavity wavelength to be long relative to the extent of the system), the rotating wave approximation (neglecting rapidly oscillating terms in the Hamiltonian - very common in quantum optics) and the dipole approximation [24]. For a molecule coupled to an optical cavity with a single optical mode of frequency ω_c ,

$$\hat{H}_{\text{PF}} = \hat{H}_{\text{mol}}(\hat{p}, \hat{q}) + \hat{H}_{\text{cav}}(\hat{p}_c, \hat{q}_c, \hat{\mu}), \quad (3.5)$$

where

$$\hat{H}_{\text{cav}} = \frac{\hat{p}_c^2}{2} + \frac{1}{2}\omega_c^2 \left(\hat{q}_c + \sqrt{\frac{2}{\hbar\omega_c}}\eta_c\hat{\mu} \right)^2, \quad (3.6)$$

which describes the optical cavity and its interaction with the system. Here, $\hat{\mu}(\hat{q}) = \hat{\mathbf{e}} \cdot \hat{\boldsymbol{\mu}}$ and is the dipole moment operator projected onto the electronic ground state, along the cavity polarisation $\hat{\mathbf{e}}$. In agreement with Lindoy *et al.* we select the dipole moment to be linear in the molecular coordinate such that $\hat{\mu} = \hat{q}$. The system–cavity coupling constant is $\eta_c = \frac{1}{\omega_c} \sqrt{\frac{\hbar\omega_c}{2\epsilon_0 V}}$, where ϵ_0 is the system permittivity and V is the system volume. For a Fabry–Pérot optical cavity, $\omega_c \propto V^{-1}$, hence making $|\eta_c|$ independent of cavity frequency in this experimental setup. The Rabi splitting of the system of interest Ω_R is directly proportional to η_c . To keep the splitting on the order of 100 cm^{-1} we will use the same range as Lindoy *et al.* with $1.25 \times 10^{-3} \text{ a.u.} \leq \eta_c \leq 5 \times 10^{-3} \text{ a.u.}$ (see Ref. [23]).

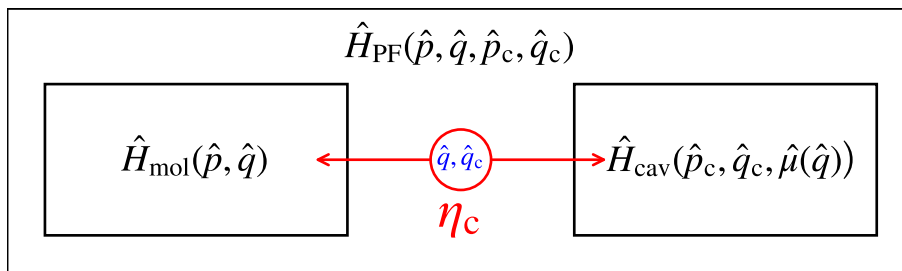


Figure 3.3: a diagram showing the possible flow of energy for an isolated quantum system comprised of an optical cavity coupled to a molecule. Red arrows indicate the flow of energy between sub-systems, blue text specifies which coordinates are linearly coupled together.

The position and momentum operators for the cavity field, \hat{p}_c and \hat{q}_c originate from the photon creation and annihilation operators \hat{a}^\dagger and \hat{a} , which are the same as those of a harmonic oscillator, and hence can be mapped to position and momentum coordinates in the same way [24].

The cavity–system coupling in Eq. (3.5) has exactly the same form as in Eq. (2.24). This means that adding an optical cavity is essentially the same as coupling the system to an additional bath with $J(\omega) \propto \delta(\omega - \omega_c)$ - a single bath mode at $\omega = \omega_c$, with a coupling strength $\propto \eta_c$.

3.3 Polariton Resonance

The final addition required for a complete model is the cavity ‘loss’ - pathways by which photons in the optical cavity are dissipated. Loss occurs due to either (i) leakage of energy due to imperfections in the mirror or (ii) interaction of the cavity with other charged particles in the surroundings.

Lindoy *et al.* used the system-bath model to simulate these effects. They introduced the parameter τ_L , the **cavity lifetime**, with which the strength of cavity loss bath was inferred.

$$\eta_L = \frac{1}{\tau_L} \frac{\omega_c^2 + \gamma_L^2}{2\gamma_L^2} (1 - e^{-\beta\hbar\omega_c}), \quad (3.7)$$

where γ_L is a parameter controlling the frequency distribution of the cavity loss, $J_L(\omega)$, as discussed in Appendix B. Adding these effects together,

$$\hat{H}_{\text{tot}} = \hat{H}_{\text{mol}}(\hat{p}, \hat{q}) + \hat{H}_{\text{bath}}(\hat{\mathbf{P}}, \hat{\mathbf{Q}}, \hat{q}) + \hat{H}_{\text{cav}}(\hat{p}_c, \hat{q}_c, \hat{\mu}) + \hat{H}_{\text{loss}}(\hat{\mathbf{P}}_c, \hat{\mathbf{Q}}_c, \hat{q}_c), \quad (3.8)$$

where \hat{H}_{mol} , \hat{H}_{bath} and \hat{H}_{cav} are as in previous sections, and

$$\hat{H}_{\text{loss}} = \sum_{i=1}^{n_l} \left[\frac{\hat{P}_{ci}^2}{2} + \frac{1}{2} \omega_{Li}^2 \left(\hat{Q}_{ci} + \frac{c_{Li}}{\omega_{Li}^2} \hat{q}_c \right)^2 \right]. \quad (3.9)$$

The notation used is the same as that of the previous sections; $\{\omega_{Bi}\}$ and $\{\omega_{Li}\}$ are the frequencies corresponding to the discretised system and cavity loss baths, with their coupling constants chosen from bath spectral densities $J_L(\omega)$ and $J_B(\omega)$ with a suitable discretisation protocol (see Appendix B).

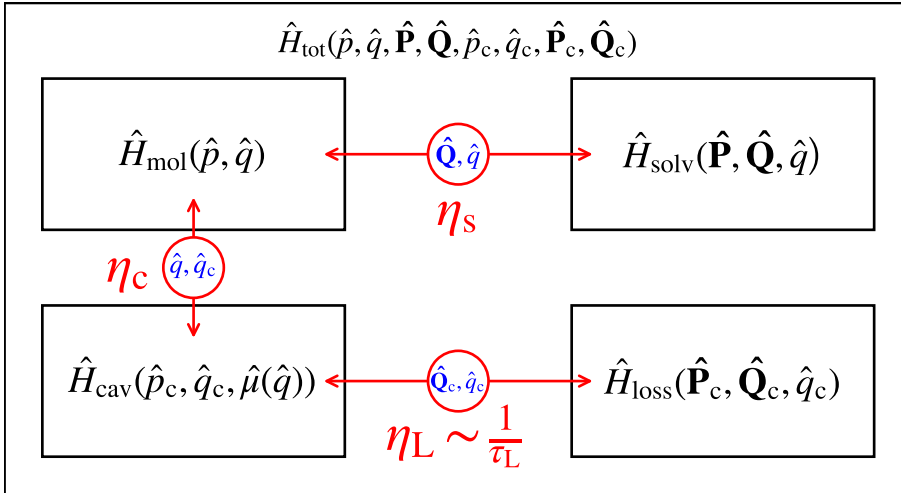


Figure 3.4: a diagram to show the possible flow of energy for an open quantum system comprised of an imperfect optical cavity coupled to a single molecule. Red arrows indicate the flow of energy, blue text indicates which coordinates are linearly coupled together

The dipole function $\hat{\mu}$ is set to equal \hat{q} for the simulations as explained in Sec. 3.2. The RPMD Hamiltonian corresponding to \hat{H}_{tot} can be formed by ‘ring polymerising’ it (as introduced in Sec. 2.2 and diagrammatically exemplified in Fig 2.2).

3.3.1 The Low Friction Regime

Setting $\eta_s/\omega_b = 0.1$ puts the system in the low friction regime, before turnover as shown in Fig. 3.2. Using the range of coupling strengths (η_c) and loss timescales (τ_L)

from Ref. [23], let us explore the effect of a cavity on the rate of reaction, varying ω_c . The effect is quantified by the dimensionless ratio, k/k_0 where k is the rate of reaction and k_0 is the corresponding rate outside the cavity (defined as that of the reaction with all parameters the same, but with $\eta_c = 0$). These results are shown in Fig. 3.5.

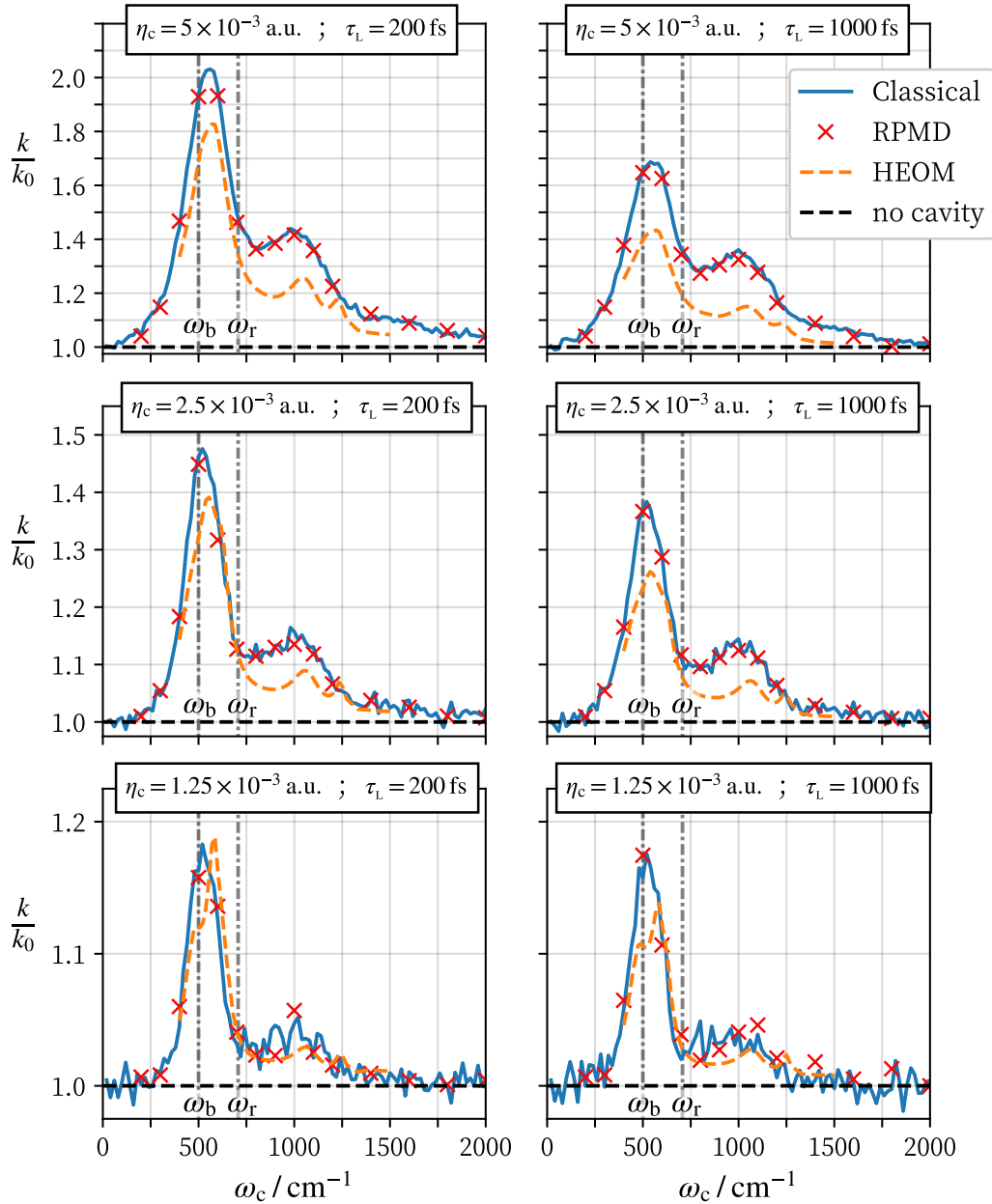


Figure 3.5: Cavity induced changes in rate in the low friction regime. The rate k is normalised by k_0 , the corresponding rate outside the cavity, defined as that of the reaction with all parameters the same, but with $\eta_c = 0$.

Somewhat surprisingly, Fig. 3.5 shows that RPMD and classical mechanics

give almost exactly the same results (to graphical accuracy) for polariton rate enhancement. This will be discussed in Sec. 3.3.3.

HEOM yields several large peaks which are captured to some extent by both 1 and 32 Bead RPMD. The peak positions do not coincide with that of the reactant frequency ω_r (which is typically the peak position observed in experiments), but are in agreement over all three methods. The peak heights, on the other hand, are found to be slightly overestimated by classical/RPMD rates compared to the HEOM results. Sec. 3.3.3 argues that the RPMD and classical cavity effects k/k_0 are the same because all of the cavity effect is in the recrossing dynamics - of which are shown to be identical in Fig. 3.7. Since this recrossing dynamics - as quantified by $c_{fs}(t)$ - is a highly nonlinear function of ω_c , simple explanations of peak widths and heights in terms of ‘resonance’ (such as those provided in experimental papers) are not supported by calculations.

Increased cavity loss, (signified by **decreased** τ_L) is found to enhance the rate of reaction. In the supplementary information of their HEOM paper, Lindoy *et al.* explored this effect, and found that the classical rate was relatively insensitive to this compared to the quantum rate. Increased cavity loss will lead to increased energy dissipation of the system via energy flow into the cavity and fast thermalisation with the loss bath (see Fig. 3.4). In this low friction regime, the increased rate of energy dissipation will increase the rate as expected by Kramer’s Theory.

HEOM’s peak heights decrease in magnitude at a slower rate as η_c is decreased, and are more effected by cavity loss than the other rate theories used. This suggests that some aspect of coherent recrossing effects [22] is contributing to the rate, which cannot be captured by RPMD (or classical MD).

3.3.2 The High Friction Regime

In the high friction regime, transition state theory is a suitable method to calculate rates due to the almost complete suppression of recrossing.

Multiple groups have investigated the cavity rate problem using various transition state theories, including Yang and Cao who used Harmonic Transition State Theory (HTST) [25]. They considered a simpler Hamiltonian without solvent interactions or cavity loss;

$$\hat{H}_{\text{Cao}} = \hat{H}_{\text{mol}} + \hat{H}_{\text{cav}} = \left[\frac{\hat{p}^2}{2} + \hat{V}(\hat{q}) \right] + \left[\frac{\hat{p}_c^2}{2} + \frac{1}{2}\omega_c^2(\hat{q}_c + g\hat{q})^2 \right]. \quad (3.10)$$

The unitless light-matter coupling constant, $g \propto \sqrt{\frac{1}{\omega_c}}$, giving the same scaling dependence of coupling with cavity frequency as in the previous model. For this reason, Eq. (3.10) corresponds to the $\eta_s = \eta_L = 0$ limit of the model depicted in Fig. 3.4. They found that the cavity only leads to a small $\sim 1\%$ decrease in reaction rate over a broad range of ω_c , with no indication of ‘resonance’ with either ω_b or ω_r .

In Fig. 3.6, we investigate if these results change when explicitly including solvent friction and cavity loss. The exact same parameters as in the previous section are used, but now with $\eta_s/\omega_b = 4$ to explore polariton rate effects in the high friction regime. The effect of the cavity on the rate is found to be tiny compared to the low-friction case. For this reason, despite using many (2×10^5) samples for transition state theory, the statistical errors of the full TST results (both classical and quantum) are almost as large as the effect itself. Nevertheless, the results indicate that there is no substantial difference between full TST and HTST, which is free of statistical errors. In either case, the effect of the cavity is small enough to say that the model does not explain experimental findings.

Also note that the rate suppression occurs over a broad range of frequencies rather than at a sharp resonance frequency. In other words, Cao’s results for the simpler model are essentially unchanged by including solvent friction and cavity loss.

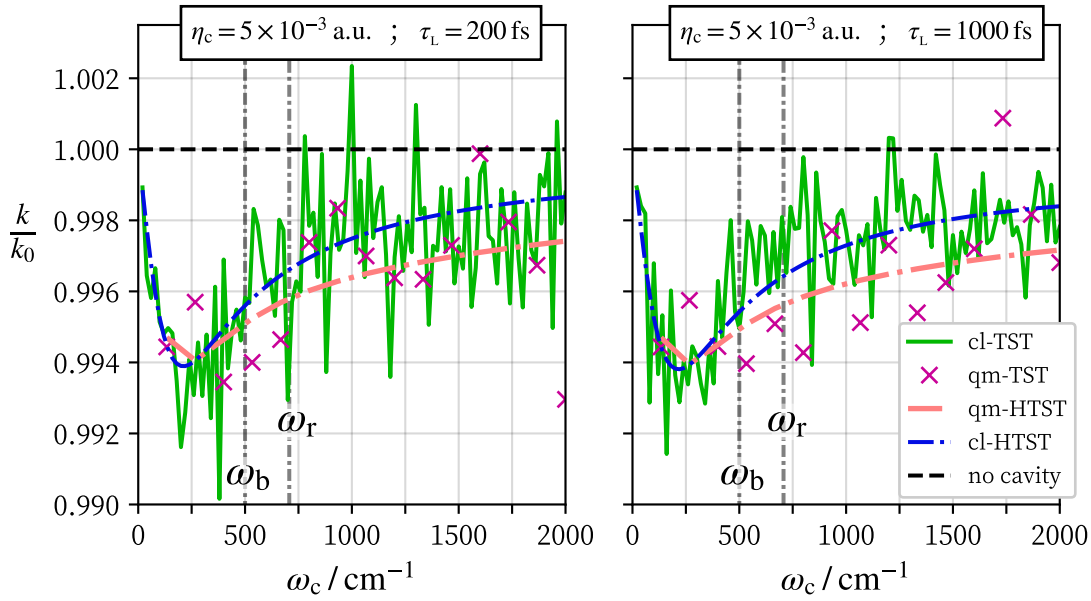


Figure 3.6: Cavity induced changes in rate in the high friction regime. The rate k is normalised by k_0 , the corresponding rate outside the cavity, defined as that of the reaction with all parameters the same, but with $\eta_c = 0$.

3.3.3 Recrossing Effects on Reaction Rates

The results of Fig. 3.5 and Fig. 3.6 imply that the main contribution to cavity-induced reaction rate adjustment can be understood entirely in terms of changes in recrossing of the dividing surface. This is quantified by the recrossing coefficient,

$$\kappa = k/k_{\text{TST}}, \quad (3.11)$$

the ratio between the flux-side rate (which includes recrossing) and the transition state theory rate (which does not). Addition of an optical cavity to the system can be seen as addition of an extra bath mode, as discussed in Sec. 3.2. As a consequence, the solvent friction is effectively increased when the cavity is added. This increases κ when in the low-friction regime by the same amount (as shown in Fig. 3.7) for **both** classical and RPMD - explaining why the rate enhancement is exactly the same, as shown in Fig. 3.5 for which $\eta_s = 0.1\omega_b$. Similarly, the cavity has little effect on the rate for $\eta_s = 4\omega_b$ in Fig. 3.6, as in this regime the cavity has a negligible effect on the amount of recrossing.

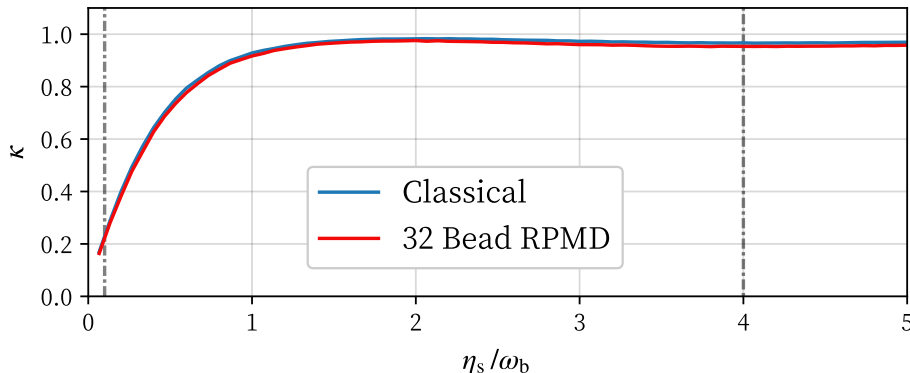


Figure 3.7: Friction dependence of κ for classical mechanics and RPMD, corresponding to the Kramer’s Turnover graph in Fig. 3.2. Dotted lines refer to the friction strengths used for the two regimes in Sec. 3.3.

3.4 Conclusions

In this chapter, we have explored polariton effects on single-molecule reactions.

We have found:

1. The RPMD and classical MD cavity effects in Fig. 3.5 (the low solvent friction regime) are similar to the exact quantum (HEOM) results for a large range of system-cavity coupling strengths and cavity loss timescales, but slightly more pronounced.
2. The quantum and classical transition state theory cavity effects in Fig. 3.6 (the high friction regime in which TST is a valid approximation - see Sec. 2.6) are negligible, consistent with Yang and Cao’s conclusion for their simpler model [25].
3. The RPMD and classical MD cavity effects in Fig. 3.5 are the same because the vast majority of the cavity effect is in the recrossing dynamics, which are the same for RPMD and classical MD as shown in Fig. 3.7. They are presumably more pronounced than the cavity effect in HEOM because of coherent effects in the HEOM recrossing dynamics (which RPMD and classical MD do not capture).

4. There is no evidence in **any** of these results for a ‘resonant’ cavity effect on the rate constant (as observed experimentally).

These conclusions of course only apply to a single reaction occurring in a single mode optical cavity, under the Hamiltonian set out in Eq. (3.8). As cavity the effect on reaction rate at high solvent friction is insignificant relative to that at low friction, the focus in the next chapter will lie solely on the low friction regime, to see if these relatively significant effects persist as the number of molecules collectively coupled to the optical cavity increases.

4

Collective Effects on Reaction Rates

Contents

4.1	Generalisation to N Reactants	33
4.2	Transition State Difficulties	34
4.3	Direct Simulation of N Reactants	36
4.3.1	The Model	38
4.3.2	Polariton Resonance in the Collective Regime	39
4.4	Conclusions	41

4.1 Generalisation to N Reactants

In this generalisation, let us assume that molecules are well separated inside of an optical cavity such that each reactant's interactions with the surroundings may be assumed to be independent. With this in mind, Eq. (3.8) can be generalised to that of N reactants by summing over the individual molecule + bath Hamiltonians, and coupling the cavity to the **total** dipole of the system;

$$\hat{H}_{\text{tot}} = \sum_{n=1}^N \left[\hat{H}_{\text{mol}}(\hat{p}_n, \hat{q}_n) + \hat{H}_{\text{bath}}(\hat{\mathbf{P}}_n, \hat{\mathbf{Q}}_n, \hat{q}_n) \right] + \hat{H}_{\text{cav}}(\hat{p}_c, \hat{q}_c, \hat{\mu}_{\text{tot}}) + \hat{H}_{\text{loss}}(\hat{\mathbf{P}}_c, \hat{\mathbf{Q}}_c, \hat{q}_c) \quad (4.1)$$

The dipole of the system, $\hat{\mu}_{\text{tot}} = \sum_{n=1}^N \hat{\mu}(\hat{q}_n) = \sum_{n=1}^N \hat{q}_n$, in analogy with the previous section. Fig. 4.1 shows the structure of this Hamiltonian diagrammatically.

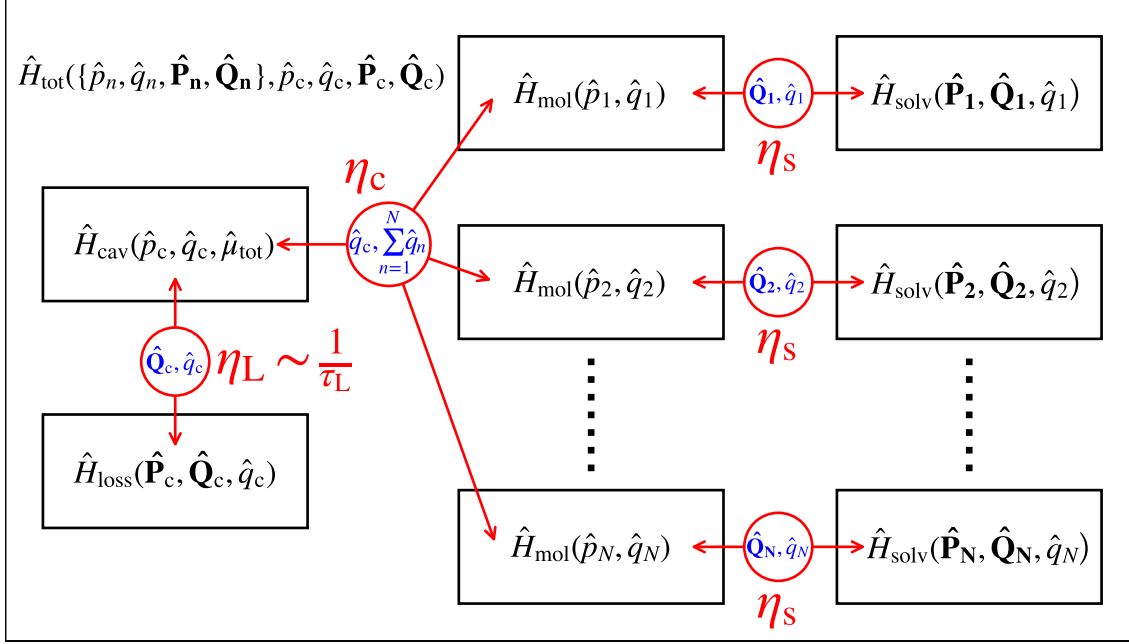


Figure 4.1: A model of the possible flow of energy for an open quantum system comprised of N molecules inside of a lossy optical cavity. Red arrows indicate the flow of energy, blue text indicates which coordinates are linearly coupled together.

4.2 Transition State Difficulties

Yang and Cao [25] have considered polariton effects on quantum rates in the collective regime. They reported a collective scaling up of polariton effect observed with centroid transition state theory, with the caveat of this requiring the polariton to be ‘activated collectively to the transition state’. In their argument, the resulting potential for N particles at the ‘collective transition state’, denoted by \ddagger_c , was approximated by a second order Taylor expansion in the normal mode basis of the molecular coordinate system;

$$V_N(\{q_n\})|_{\ddagger_c} \simeq E_a - \frac{1}{2}\omega_b^2 q_B^2 + \sum_{i=1}^{N-1} \frac{1}{2}\omega_r^2 q_{Di}^2. \quad (4.2)$$

Here, q_{Di} is the i -th ‘dark state’ (each of the $N - 1$ possible non-totally-symmetric linear combinations of the N reactant coordinates, which are uncoupled from the optical cavity; hence ‘dark’), oscillating at the single molecule reactant frequency ω_r . The barrier curvature, ω_b corresponds to that of the single molecule system, and E_a the activation energy required for this reaction pathway. The ‘bright

state at the barrier'

$$q_B = \frac{1}{\sqrt{N}} \sum_{n=1}^N q_n, \quad (4.3)$$

the totally symmetric linear combination of mass-scaled reaction coordinates of the N identical reactants. This expansion of $V(q)$ is troublesome however, as can be explained by considering the simplest case, $N = 2$. The potential energy surface for this 2-molecule system - in the absence of an optical cavity is

$$V(q_1, q_2) = V_{\text{mol}}(q_1) + V_{\text{mol}}(q_2), \quad (4.4)$$

where $V_{\text{mol}}(q)$ is a 1-dimensional double-well potential as described in Sec. 3.1, with transition state and reactant/product minima located at $q = 0$ and $q = \pm q_r$ respectively. This surface is visualised in Fig 4.2

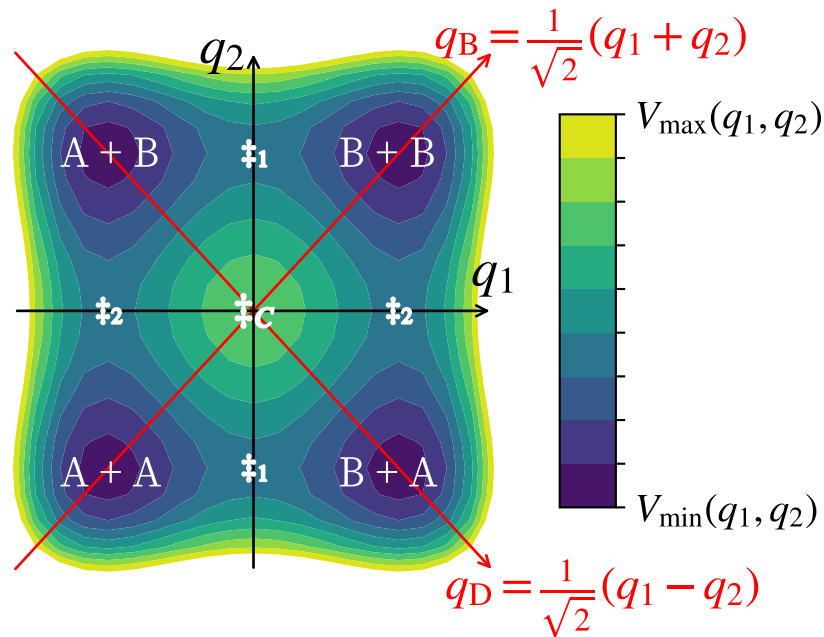


Figure 4.2: ‘Collective excitation’ requires N times larger activation energy and gives incorrect saddle-point index for ‘transition state’

The potential maximum (which would correspond to the transition state) for the collective reaction coordinate q_B is located at \ddagger_C . The activation energy required to reach this point is $E_a = V_{\text{mol}}(0) + V_{\text{mol}}(0) = 2E_b$. Due to its exponentially

smaller Boltzmann weighting, this pathway would have a negligible contribution to the reaction rate relative to ‘non-coherent’ reactions occurring via \ddagger_1 or \ddagger_2 with activation energy $E_a = V_{\text{mol}}(q_r) + V_{\text{mol}}(0) = E_b$ when uncoupled to the optical cavity. In addition, if one is to say

$$\left(\frac{\partial^2 V(q_1, q_2)}{\partial q_B^2} \right) \Big|_{\ddagger_C} = -\omega_b^2, \quad (4.5)$$

then by symmetry (as $V_{\text{mol}}(q)$ is the same function for each coordinate)

$$\left(\frac{\partial^2 V(q_1, q_2)}{\partial q_D^2} \right) \Big|_{\ddagger_C} = -\omega_b^2, \text{ not } \omega_r^2, \quad (4.6)$$

which would make this ‘transition state’ a maximum in the potential rather than a saddle point, making no physical sense. This reasoning can be extended to N reactants, in which ‘collective excitation to the transition state’ is at a maximum point in the potential, with N times the activation energy. For this reason, most if not all reactions should go via ‘non-coherent’ reaction pathways which are first order saddle points in the potential, with single-molecule activation energies.

In the same paper it was shown that the cavity effects on ‘non-coherent’ reactions decreased to zero as the number of reactants coupled to the optical cavity was increased. This therefore suggests that transition state theory is not be able to capture the ‘collective effect’ as observed experimentally, further justifying the decision to perform simulations in the low friction regime, where recrossing effects are most pronounced.

4.3 Direct Simulation of N Reactants

The ambiguities in the definition of a dividing surface for an N -molecule reactant system coupled to a cavity can be removed by simply **not imposing a collective dividing surface**. Instead, one could set up a direct simulation by sampling the Boltzmann distribution of the N reactants, then evolving and measuring the amount

of product formed as a function of time. The rate of reaction can then be inferred by fitting the uni-molecular rate constant to the population curve. This can be derived by considering the rate process



As the rate of reaction considered here corresponds to that of a symmetric double well, by detailed balance, $k_f = k_b = k$. For initial population conditions subject to the population conservation constraint, $P_A(t) + P_B(t) = 1$,

$$\dot{P}_A = k(1 - 2P_A). \quad (4.8)$$

This can be integrated, followed by applying the initial conditions $P_A(0) = 1$, to yield

$$P_A(t) = \frac{1}{2} (1 + e^{-2kt}), \quad (4.9)$$

which can be rearranged to

$$-\frac{1}{2} \ln(2P_A(t) - 1) = kt, \quad (4.10)$$

which allows the rate of reaction to be inferred via linear regression. The initial non-rate-like behaviour was found to occur for at most the first 500 fs of simulation and was therefore discarded in all data.

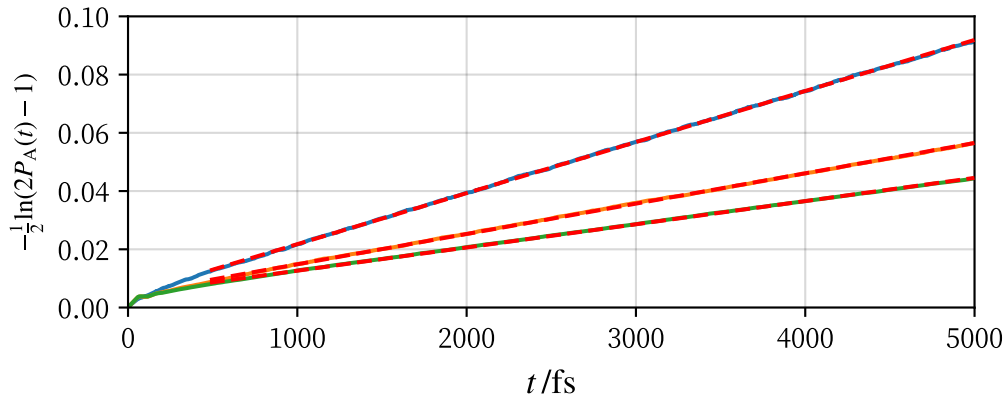


Figure 4.3: Procedure by which rate constants are obtained from population decay in direct simulation. Coloured lines represent a couple of examples of simulated data used to make Fig. 4.4, dotted red lines are linear fits used to obtain k .

In this way k can be fitted to the population curve obtained by direct simulation, to give the rate of reaction for N reactants coupled to an optical cavity without the need for any arbitrary definition of a collective dividing surface.

4.3.1 The Model

The simulation was divided into two stages. As the results obtained with RPMD in Ch. 3 were very similar to classical mechanics, the methods used were purely classical (for computational ease).

Stage 1: Equilibrium sampling of reactant configurations. This was done by a molecular dynamics simulation with the Hamiltonian of Eq. (4.1), but with all trajectories constrained such that barrier crossing was prohibited. This was achieved by altering the potential energy surface in H_{mol} such that

$$V_{\text{mol}}(q) \leftarrow \begin{cases} V_{\text{mol}}(q) & \left(= \frac{\omega_{\text{b}}^4}{16E_{\text{b}}}q^4 - \frac{\omega_{\text{b}}^2}{2}q^2 \right) & \text{if } q \leq 0 \\ \infty & & \text{if } q > 0 \end{cases} \quad (4.11)$$

This effectively installed an elastic barrier at the dividing surface, $q = 0$, ‘bouncing’ all barrier-crossing trajectories back into the reactant well. At regular interval of 100 fs (to get uncorrelated samples), the coordinates and momenta of all particles were recorded and stored.

Stage 2: Simulation of reactant trajectories. Each sample taken in the previous stage was then used as a set of initial conditions for an unconstrained simulation (i.e. with no infinite barrier in at $q = 0$). Molecular dynamics was then used to progress these conditions in time. After each time-step the fraction of molecules on each side of the dividing surface was measured. Explicitly, this defines the population of reactants as

$$p_{\text{A}}(t) = \frac{1}{N_{\text{s}}} \sum_{s=1}^{N_{\text{s}}} \left(\frac{1}{N} \sum_{n=1}^N \theta \left(-q_n^{(s)}(t) \right) \right) \quad (4.12)$$

and the population of products as

$$p_B(t) = \frac{1}{N_s} \sum_{s=1}^{N_s} \left(\frac{1}{N} \sum_{n=1}^N \theta(q_n^{(s)}(t)) \right), \quad (4.13)$$

where $\theta(x)$ is a Heaviside step function, N_s is the number of samples obtained in stage 1 and N the number of reactants coupled to the cavity as specified in the Hamiltonian. In contrast with the single-molecule studies, in which the simulation temperature was set to 300 K, the temperature was **elevated to 500 K** for these direct simulations. This was done to make barrier crossing more frequent and as such allow both shorter simulations with fewer samples.

To minimise the computational cost of simulation of many degrees of freedom (recall that each molecule is connected to its own solvent bath), the system-bath dynamics were integrated using the generalised Langevin equations (GLE) (see Appendix B). These effectively replaced each bath with a single degree of freedom which evolved stochastically and thereby mimicked the effect of friction on the system.

4.3.2 Polariton Resonance in the Collective Regime

As mentioned in the introduction, the Rabi splitting of an infrared band in resonance with a cavity mode serves as a simple measurement of the light-matter coupling,

$$\Omega_R \propto \eta_c \sqrt{N}. \quad (4.14)$$

To isolate the effect of changing the number of molecules for a constant Rabi splitting, we scale down η_c by \sqrt{N} for an ensemble of molecules to keep $\eta_c \sqrt{N}$ constant. As $N \rightarrow \infty$, the coupling constant will of course tend 0. The important question is though: as one approaches the collective regime where N is on the order of 10^{10} , will the cavity effects persist?

To answer this question the top left panel of Fig. 3.5 was reproduced, but now with the temperature at 500 K (and all other parameters kept exactly the same). The same reaction was then simulated using the procedure outlined in

Sec 4.3.1, followed by subsequent simulations with an increased number of molecules, for a constant Rabi splitting.

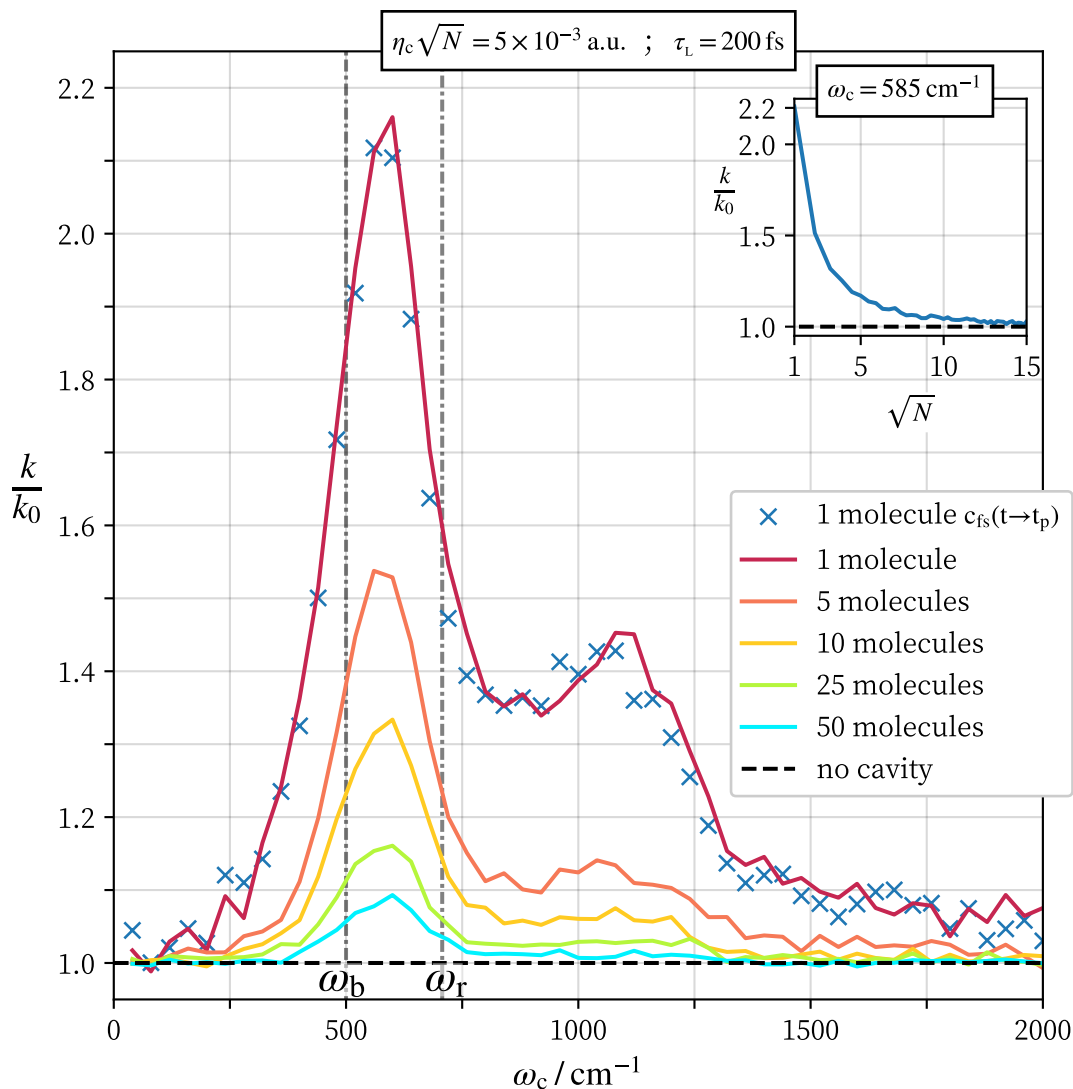


Figure 4.4: Collective polariton resonance in low-friction regime ($\eta_s/\omega_b = 0.1$) at an elevated temperature of 500 K. Solid lines denote results obtained using direct simulation. Crosses are used for flux-side correlation results. The inset figure shows the maximal effect on reaction rates - found to be for $\omega_c = 585 \text{ cm}^{-1}$ - decreasing to zero over an even larger range of N .

First, we confirm that classical rate theory ($c_{fs}(t \rightarrow t_p)$) agrees almost perfectly with the direct simulation, shown in Fig. 4.4 by the overall agreement between blue crosses and red line. As expected, we find that the effect of the cavity on each system decreases as the N is increased, for a constant Rabi splitting. The peak positions seem to be unchanged throughout. The inset figure shows the decrease in

maximum peak height with an even larger range of N , implying that as N approaches experimentally realistic values, the cavity rate enhancement will be negligible. If it is assumed that all relevant effects are captured to some extent by the methods used here, then the Hamiltonian must be insufficient in its description of chemical reactions occurring in an optical cavity. This is a startling conclusion, considering that it is widely used in literature [26, 27, 28].

4.4 Conclusions

In retrospect, it is relatively unsurprising that the optical cavity’s effect on a single molecule’s properties vanishes as N increases. This is due to the fact that the optical cavity couples to the **total** dipole of the system.

$$\hat{\mu}_{\text{tot}} = \sum_{n=1}^N \hat{\mu}(\hat{q}_n), \quad (4.15)$$

which under the Pauli–Fierz Hamiltonian of 3.2 gives a light-matter interaction potential

$$\hat{V}_{\text{cav}}(q_c, \mu_{\text{tot}}) = \frac{1}{2} \omega_c^2 \left(\hat{q}_c + \sqrt{\frac{2}{\omega_c}} \eta_c \sum_{n=1}^N \hat{\mu}(\hat{q}_n) \right)^2. \quad (4.16)$$

The cavity is therefore only coupled to one linear (the totally symmetric) combination of the dipoles of the individual reactants. This is also shown diagrammatically in Fig. 4.1. In other words, the interaction strength per molecule is reduced by a factor of \sqrt{N} for a constant Rabi splitting for N molecules, causing all cavity effects to be ‘scaled out’ in the collective regime.

The cavity affects the bulk infrared absorption spectrum of the system as a whole, but as the number of degrees of freedom is increased, the effect on each individual molecule decreases, as shown by Fig. 4.4, and therefore with this Hamiltonian the introduction of an optical cavity will not affect any single-molecule properties of a bulk system. This section has used a classical theory, but due to the fact that HEOM found the same qualitative behaviour as shown in Fig. 3.5, I expect the scaling-out

argument to apply also in full quantum mechanics. This chapter concludes the exploration into polariton effects on chemical reaction rates. The next chapter discusses possible polariton effects on equilibria, attacking the problem from a more theoretical standpoint, now using quantum statistical mechanics.

5

Cavity Effects on Equilibrium Constants

Contents

5.1	Single-Molecule Effects	44
5.2	<i>N</i>-Molecule Effects	47
5.3	Simulation	51

The equilibrium constant of the charge-transfer complexation between mesitylene and iodine, when occurring within an optical cavity, has been reported [7] to either double or decrease by four times simply depending on which infrared active vibrational degree of freedom the cavity was in resonance with. Similar results have been reported for benzene and iodine. To explore these effects let us consider a unimolecular equilibrium process,



The equilibrium constant is defined as

$$K = \frac{k_f}{k_b} = \frac{Q_B}{Q_A}, \quad (5.2)$$

where Q_A and Q_B correspond to the molecular partition functions of A and B. This

ratio can also be expressed in terms of probabilities,

$$K = \frac{p_B}{p_A}, \quad (5.3)$$

where p_A and p_B are the probabilities of being in state A and B. This chapter will explore cavity effects on equilibria, firstly from a theoretical standpoint, followed by a simulation.

5.1 Single-Molecule Effects

First, we define p_A and p_B in statistical mechanics. Consider a single molecular system in the absence of an optical cavity. For a dividing surface located at $q = 0$, the reactant (A) projection operator is

$$\hat{\theta}_A = \theta(-\hat{q}), \quad (5.4)$$

and product (B) operator is

$$\hat{\theta}_B = \theta(\hat{q}), \quad (5.5)$$

where $\theta(x)$ is the Heaviside step function. As the reaction can yield either A or B,

$$\hat{\theta}_A + \hat{\theta}_B = \hat{\mathbb{1}}. \quad (5.6)$$

For a quantum system comprised of a single molecular sub-system coupled to an optical cavity, the product basis states are

$$|q_c q\rangle = |q_c\rangle \otimes |q\rangle. \quad (5.7)$$

In the combined cavity-molecule system, the reactant projector is

$$\hat{h}_A = \hat{\mathbb{1}} \otimes \hat{\theta}_A, \quad (5.8)$$

with \hat{h}_B defined analogously. Again, $\hat{h}_A + \hat{h}_B = \hat{\mathbb{1}} \otimes \hat{\mathbb{1}}$. The probability of A can therefore be expressed as a trace over the entire molecule-cavity space as

$$p_A = \frac{\text{Tr}\{e^{-\beta\hat{H}}\hat{h}_A\}}{Q}, \quad (5.9)$$

where the total partition function of the system is

$$Q = \text{Tr}\{e^{-\beta\hat{H}}\}, \quad (5.10)$$

and \hat{H} is the total cavity-molecule Hamiltonian as defined in Eq. (3.5). The probability of B is defined analogously. From Eq. (5.3), the equilibrium constant for this reaction is therefore

$$K = \frac{\text{Tr}\{e^{-\beta\hat{H}}\hat{h}_B\}}{\text{Tr}\{e^{-\beta\hat{H}}\hat{h}_A\}}. \quad (5.11)$$

Focusing our attention to the numerator,

$$\text{Tr}\{e^{-\beta\hat{H}}\hat{h}_A\} = \int_{-\infty}^{\infty} dq_c \int_{-\infty}^{\infty} dq \langle q_c q | e^{-\beta\hat{H}} \hat{h}_A | q_c q \rangle. \quad (5.12)$$

By applying the Heaviside step function, the limits of this integral are changed such that

$$\text{Tr}\{e^{-\beta\hat{H}}\hat{h}_A\} = \int_{-\infty}^{\infty} dq_c \int_{-\infty}^0 dq \langle q_c q | e^{-\beta\hat{H}} | q_c q \rangle. \quad (5.13)$$

At room temperature, $k_B T \approx 200 \text{ cm}^{-1}$. For the double-well model of the past chapters, the barrier height is $E_b = 2000 \text{ cm}^{-1}$, meaning that the position distribution in A is heavily localised about the reactant potential minimum. Near this minimum, the potential is locally harmonic. Hence at ambient temperatures, the position distribution can be approximated as Gaussian such that,

$$\text{Tr}\{e^{-\beta\hat{H}}\hat{h}_A\} \approx \int_{-\infty}^{\infty} dq_c \int_{-\infty}^{\infty} dq \langle q_c q | e^{-\beta(\hat{H}_A + \hat{H}_{\text{cavA}})} | q_c q \rangle, \quad (5.14)$$

where

$$\hat{H}_A = \frac{\hat{p}^2}{2} + E_A + \frac{1}{2}\omega_A^2 \hat{q}^2, \quad (5.15)$$

in which $E_A + \frac{1}{2}\omega_A^2 \hat{q}^2$ is the second order Taylor expansion of $\hat{V}(\hat{q})$ about the reactant minimum. Note that we have returned the upper limit of the integral over q in Eq. (5.14) to infinity. This is valid because once we have made the harmonic approximation to the reactant potential in (5.15) the Boltzmann probability

distribution in q will be negligible for $q > 0$. The approximation (5.14) improves as $\beta E_b \rightarrow \infty$, due to increased localisation of this Boltzmann position distribution. Note also that this simple one-dimensional model can easily be generalised to multiple degrees of freedom by adding an index to \hat{q} and replacing $\omega_A^2 \hat{q}^2$ by the appropriate quadratic form involving the Hessian of the multidimensional potential surface. Just as in previous sections,

$$\hat{H}_{\text{cavA}}(\hat{p}_c, \hat{q}_c, \hat{\mu}(\hat{q})) = \frac{\hat{p}_c^2}{2} + \frac{1}{2}\omega_c^2 (\hat{q}_c + g_A \hat{q})^2, \quad (5.16)$$

in which the constant g_A is the effective light-matter coupling constant at the reactant minimum. To perform the integral (5.14), we diagonalise

$$\mathbf{V}_A'' = \begin{pmatrix} \omega_c^2 & g_A \omega_c^2 \\ g_A \omega_c^2 & \omega_A^2 + g_A^2 \omega_c^2 \end{pmatrix}, \quad (5.17)$$

the Hessian matrix of $\hat{H}_A + \hat{H}_{\text{cavA}}$. The eigenvalues of this matrix are

$$\Omega_{A\pm}^2 = \frac{1}{2} (\omega_A^2 + g_A^2 \omega_c^2 + \omega_c^2) \pm \frac{1}{2} \sqrt{(\omega_A^2 + g_A^2 \omega_c^2 - \omega_c^2)^2 + 4g_A^2 \omega_c^4}. \quad (5.18)$$

As the diagonalisation is a unitary transformation, the integral (5.14) can be transformed with a unit Jacobian, allowing it to be expressed in terms of the product of partition functions of uncoupled harmonic oscillators of frequencies $\Omega_{A\pm}$, with a constant energy shift E_A . The same is of course true for B.

The quantum-mechanical equilibrium constant for a polariton system, using Eq. (2.33) is therefore

$$K = \frac{\sinh(\beta\hbar\Omega_{A-}/2) \sinh(\beta\hbar\Omega_{A+}/2)}{\sinh(\beta\hbar\Omega_{B-}/2) \sinh(\beta\hbar\Omega_{B+}/2)} e^{-\beta(E_B - E_A)}. \quad (5.19)$$

Hence, for a (quantum) single molecular system, an optical cavity **can** effect equilibrium constants. This is true though only if either $\omega_A \neq \omega_B$ or $g_A \neq g_B$. Otherwise we would have that $\Omega_{A\pm} = \Omega_{B\pm}$, and the cavity effect would cancel.

Taking the classical $\beta \rightarrow 0$ limit of (5.19) gives

$$K^{\text{cl}} = \frac{\Omega_{A+}\Omega_{A-}}{\Omega_{B+}\Omega_{B-}} e^{-\beta(E_B - E_A)}, \quad (5.20)$$

which, after inserting Eq. (5.18) for each Ω , simplifies to

$$K^{\text{cl}} = \frac{\omega_A}{\omega_B} e^{-\beta(E_B - E_A)}, \quad (5.21)$$

which is the equilibrium constant of the reaction uncoupled from the optical cavity. This shows that while an optical cavity may effect quantum-mechanical equilibrium constants, it will have no effect classically. The main question though is will the effect on the quantum equilibrium constant survive in the collective limit?

5.2 N -Molecule Effects

For a system containing N reactions, the probability that a given reaction selected at random is in A is given by the projection operator

$$\hat{h}_A = \frac{1}{N} \sum_{i=1}^N \hat{h}_{Ai}, \quad (5.22)$$

which is constructed from the projection operator of each subsystem into state A, such that $\hat{h}_A + \hat{h}_B = \hat{\mathbb{1}}$ just as for the $N = 1$ case. Using statistical mechanics, the probability of A is therefore written as

$$p_A = \frac{\text{Tr}\{e^{-\beta\hat{H}}\hat{h}_A\}}{Q}. \quad (5.23)$$

For a product basis defined by

$$|q_c q_1 q_2 \dots q_N\rangle = |q_c\rangle \otimes |q_1\rangle \otimes |q_2\rangle \dots \otimes |q_N\rangle, \quad (5.24)$$

these projection operators

$$\hat{h}_{Ai} = \hat{\mathbb{1}} \otimes \underbrace{\hat{\mathbb{1}} \otimes \dots \otimes \hat{\mathbb{1}}}_{i-1 \text{ factors}} \otimes \hat{\theta}_A \otimes \underbrace{\hat{\mathbb{1}} \otimes \dots \otimes \hat{\mathbb{1}}}_{N-i \text{ factors}}, \quad (5.25)$$

with $\hat{\theta}_A$ defined exactly as in the previous section. Eq. (5.6) can now be inserted into all identities corresponding to molecular coordinates such that,

$$\hat{h}_{Ai} = \hat{\mathbb{1}} \otimes \underbrace{(\hat{\theta}_A + \hat{\theta}_B) \otimes \dots \otimes (\hat{\theta}_A + \hat{\theta}_B)}_{i-1 \text{ factors}} \otimes \hat{\theta}_A \otimes \underbrace{(\hat{\theta}_A + \hat{\theta}_B) \otimes \dots \otimes (\hat{\theta}_A + \hat{\theta}_B)}_{N-i \text{ factors}}. \quad (5.26)$$

As each individual molecular Hamiltonian is the same, the labelling of particles does not matter. Therefore a rearrangement of the molecular projection operators is permitted such that,

$$\hat{h}_A = \frac{1}{N} \sum_{i=1}^N \hat{\mathbf{1}} \otimes \underbrace{(\hat{\theta}_A + \hat{\theta}_B) \otimes \dots \otimes (\hat{\theta}_A + \hat{\theta}_B)}_{N-1 \text{ factors}} \otimes \hat{\theta}_A, \quad (5.27)$$

which is a sum over N similar terms, allowing us to remove the sum and divide by N . Then, using the Binomial theorem,

$$\hat{h}_A = \hat{\mathbf{1}} \otimes \sum_{r=0}^{N-1} \binom{N-1}{r} \underbrace{\hat{\theta}_A \otimes \dots \otimes \hat{\theta}_A}_{r+1 \text{ factors}} \otimes \underbrace{\hat{\theta}_B \otimes \dots \otimes \hat{\theta}_B}_{N-(r+1) \text{ factors}}, \quad (5.28)$$

which after rearranging can be written more simply as

$$\hat{h}_A = \hat{\mathbf{1}} \otimes \sum_{r=0}^N \binom{N}{r} \frac{r}{N} \underbrace{\hat{\theta}_A \otimes \dots \otimes \hat{\theta}_A}_r \otimes \underbrace{\hat{\theta}_B \otimes \dots \otimes \hat{\theta}_B}_{N-r}. \quad (5.29)$$

The numerator of Eq. (5.23) can therefore be expressed as an integral of the Boltzmann operator over a constrained space, just as in Eq. (5.13) such that

$$\begin{aligned} \text{Tr}\{e^{-\beta\hat{H}}\hat{h}_A\} &= \sum_{r=0}^N \binom{N}{r} \frac{r}{N} \int_{-\infty}^{\infty} dq_c \prod_{j=1}^r \left(\int_{-\infty}^0 dq_j \right) \prod_{j=r+1}^N \left(\int_0^{\infty} dq_j \right) \\ &\quad \times \langle q_c \ q_1 \ q_2 \ \dots \ q_N | e^{-\beta\hat{H}} | q_c \ q_1 \ q_2 \ \dots \ q_N \rangle. \end{aligned} \quad (5.30)$$

Now we can apply the same harmonic approximation as was made to yield Eq. (5.14), but now over N directions (corresponding to each integral over either A or B) such that

$$\text{Tr}\{e^{-\beta\hat{H}}\hat{h}_A\} \approx \sum_{r=0}^N \binom{N}{r} \frac{r}{N} \text{Tr}\{e^{-\beta\hat{H}_r}\}, \quad (5.31)$$

where \hat{H}_r is the Hamiltonian corresponding to a system of N reaction coordinates, the first r of which are on side A and the other $N-r$ of which are on side B, coupled to an optical cavity.

Let us now focus on the potential of \hat{H}_r , for which N harmonic approximations have been made such that

$$\begin{aligned} \hat{V}_r &= rE_A + \frac{1}{2}\omega_A^2 \sum_{j=1}^r \hat{q}_j^2 + (N-r)E_B + \frac{1}{2}\omega_B^2 \sum_{j=r+1}^N \hat{q}_j^2 \\ &\quad + \frac{1}{2}\omega_c^2 \left(\hat{q}_c + g_A \sum_{j=1}^r \hat{q}_j + g_B \sum_{j=r+1}^N \hat{q}_j \right)^2. \end{aligned} \quad (5.32)$$

Via two unitary transforms, one can rotate into the ‘dark’/‘bright’ modes of coordinates confined in wells A and B. For those in A,

$$\hat{q}_{Ak} = \frac{1}{\sqrt{r}} \sum_{j=1}^r e^{\frac{2\pi i}{r}kj} \hat{q}_j \quad k = 0, 1, 2 \dots r-1, \quad (5.33)$$

and those in B,

$$\hat{q}_{Bk} = \frac{1}{\sqrt{N-r}} \sum_{j=1}^{N-r} e^{\frac{2\pi i}{N-r}lj} \hat{q}_{j+r} \quad k = 0, 1, 2 \dots N-r-1. \quad (5.34)$$

For both, $k = 0$ corresponds to the totally symmetric linear combination of coordinates, which is commonly known as the ‘bright state’ due to the fact this is the only linear combination that interacts with the optical cavity. As this is a unitary transformation, inner product is conserved such that the potential can be written in the new coordinates as

$$\begin{aligned} \hat{V}_r = rE_A + \frac{1}{2}\omega_A^2 \sum_{k=0}^{r-1} \hat{q}_{Ak}^2 + (N-r)E_B + \frac{1}{2}\omega_B^2 \sum_{k=0}^{N-r-1} \hat{q}_{Bk}^2 \\ + \frac{1}{2}\omega_c^2 \left(\hat{q}_c + g_A\sqrt{r} \hat{q}_{A0} + g_B\sqrt{N-r} \hat{q}_{B0} \right)^2. \end{aligned} \quad (5.35)$$

This now means that \hat{H}_r can be factored into

$$\hat{H}_r = \sum_{k=1}^{r-1} \hat{H}_A(\hat{p}_{Ak}, \hat{q}_{Ak}) + \sum_{k=1}^{N-r-1} \hat{H}_B(\hat{p}_{Bk}, \hat{q}_{Bk}) + \hat{H}_r^{\text{bright}}, \quad (5.36)$$

where H_A and H_B are the Hamiltonians of A and B for a single molecular system uncoupled from the optical cavity as defined in Eq. (5.15), and

$$\hat{H}_r^{\text{bright}} = \frac{\hat{p}_{A0}^2}{2} + \frac{\hat{p}_{B0}^2}{2} + \frac{\hat{p}_c^2}{2} + \hat{V}_r^{\text{bright}}, \quad (5.37)$$

in which

$$\begin{aligned} \hat{V}_r^{\text{bright}} = E_A + \frac{1}{2}\omega_A^2 \hat{q}_{A0}^2 + E_B + \frac{1}{2}\omega_B^2 \hat{q}_{B0}^2 + \\ \frac{1}{2}\omega_c^2 \left(\hat{q}_c + g_A\sqrt{r} \hat{q}_{A0} + g_B\sqrt{N-r} \hat{q}_{B0} \right)^2. \end{aligned} \quad (5.38)$$

Inserting Eq. (5.38) back into the Eq. (5.31), tracing over all uncoupled dark states - yielding the molecular partition functions $Q_A = \text{Tr}\{e^{-\beta\hat{H}_A}\}$ and $Q_B = \text{Tr}\{e^{-\beta\hat{H}_B}\}$ - we have

$$\text{Tr}\{e^{-\beta\hat{H}} \hat{h}_A\} \approx \sum_{r=0}^N \binom{N}{r} \frac{r}{N} Q_A^{r-1} Q_B^{N-r-1} \text{Tr}\{e^{-\beta\hat{H}_r^{\text{bright}}}\}. \quad (5.39)$$

The concentration of B can be expressed in an analogous form such that the equilibrium constant is

$$K = \frac{\sum_{r=0}^N \binom{N}{r} r Q_B^{r-1} Q_A^{N-r-1} \text{Tr}\left\{e^{-\beta \hat{H}_{N-r}^{\text{bright}}}\right\}}{\sum_{r=0}^N \binom{N}{r} r Q_A^{r-1} Q_B^{N-r-1} \text{Tr}\left\{e^{-\beta \hat{H}_r^{\text{bright}}}\right\}}. \quad (5.40)$$

Now let us introduce $r' = N - r$ into the upper sum,

$$K = \frac{\sum_{r'=0}^N \binom{N}{N-r'} (N-r') Q_B^{N-r'-1} Q_A^{r'-1} \text{Tr}\left\{e^{-\beta \hat{H}_{r'}^{\text{bright}}}\right\}}{\sum_{r=0}^N \binom{N}{r} r Q_A^{r-1} Q_B^{N-r-1} \text{Tr}\left\{e^{-\beta \hat{H}_r^{\text{bright}}}\right\}}. \quad (5.41)$$

Removing the prime, and cancelling the factors of Q_A and Q_B ,

$$K = \frac{\sum_{r=0}^N \binom{N}{r} (N-r) \left(\frac{Q_A}{Q_B}\right)^r \text{Tr}\left\{e^{-\beta \hat{H}_r^{\text{bright}}}\right\}}{\sum_{r=0}^N \binom{N}{r} r \left(\frac{Q_A}{Q_B}\right)^r \text{Tr}\left\{e^{-\beta \hat{H}_r^{\text{bright}}}\right\}}. \quad (5.42)$$

In analogy with the previous section, we diagonalise the Hessian of the ‘bright-mode’ Hamiltonian

$$\mathbf{V}_r'' = \begin{pmatrix} \omega_A^2 + r\omega_c^2 g_A^2 & \sqrt{r(N-r)} g_A g_B \omega_c^2 & \sqrt{r} g_A \omega_c^2 \\ \sqrt{r(N-r)} g_A g_B \omega_c^2 & \omega_B^2 + (N-r)\omega_c^2 g_B^2 & \sqrt{N-r} g_B \omega_c^2 \\ \sqrt{r} g_A \omega_c^2 & \sqrt{N-r} g_B \omega_c^2 & \omega_c^2 \end{pmatrix}, \quad (5.43)$$

in the basis

$$|q_{A0} q_{B0} q_c\rangle = |q_{A0}\rangle \otimes |q_{B0}\rangle \otimes |q_c\rangle, \quad (5.44)$$

to yield eigenvalues $\{\lambda_{r1}^2, \lambda_{r2}^2, \lambda_{r3}^2\}$. Using these, and the quantum harmonic oscillator partition functions just as in the previous section,

$$\text{Tr}\left\{e^{-\beta \hat{H}_r^{\text{bright}}}\right\} = \prod_{i=1,2,3} \left[\frac{1}{2 \sinh(\beta \hbar \lambda_{ri}/2)} \right] e^{-\beta(E_A + E_B)}, \quad (5.45)$$

which can be inserted into Eq. (5.42) so that

$$K = \frac{\sum_{r=0}^N \binom{N}{r} (N-r) \left(\frac{Q_A}{Q_B}\right)^r \prod_{i=1,2,3} \left[\frac{1}{\sinh(\beta \hbar \lambda_{ri}/2)} \right]}{\sum_{r=0}^N \binom{N}{r} r \left(\frac{Q_A}{Q_B}\right)^r \prod_{i=1,2,3} \left[\frac{1}{\sinh(\beta \hbar \lambda_{ri}/2)} \right]}. \quad (5.46)$$

Finally, one can notice that the ratio of single molecule uncoupled partition functions is the equilibrium constant of the reaction outside of a cavity, K_0 giving our final expression

$$K = \frac{\sum_{r=0}^N \binom{N}{r} (N-r) K_0^{-r} B(r)}{\sum_{r=0}^N \binom{N}{r} r K_0^{-r} B(r)}, \quad (5.47)$$

where

$$B(r) = \prod_{i=1,2,3} \left[\frac{1}{\sinh(\beta \hbar \lambda_{ri}/2)} \right]. \quad (5.48)$$

In Appendix D it is shown that Eq. (5.47) reduces to K_0 when uncoupled from an optical cavity. The classical $\beta \rightarrow 0$ limit of K ,

$$K^{\text{cl}} = \frac{\sum_{r=0}^N \binom{N}{r} (N-r) K_0^{-r} \left[\frac{1}{\det \mathbf{V}_r''} \right]^{\frac{1}{2}}}{\sum_{r=0}^N \binom{N}{r} r K_0^{-r} \left[\frac{1}{\det \mathbf{V}_r''} \right]^{\frac{1}{2}}}, \quad (5.49)$$

which, due to the fact that

$$\det \mathbf{V}_r'' = \omega_A^2 \omega_B^2 \omega_c^2, \quad (5.50)$$

can be simplified to

$$K^{\text{cl}} = K_0. \quad (5.51)$$

Therefore - as expected from the single reactant case - the optical cavity will have no effect on the equilibrium constant of a system of N reactions in the classical limit. This observation is corroborated by the findings of Li *et al.* in Ref. [29], who gave a proof that in the classical limit the cavity will not effect any static equilibrium properties of a system within. For the quantum case though there may be some effect, according to Eq. (5.47). This will now be numerically tested.

5.3 Simulation

One could consider the cavity effects on the equilibrium constant of the symmetric double-well from the previous chapters. However, due to the symmetry of the

potential energy surface, $\omega_A = \omega_B$ and $g_A = g_B$, meaning that no effects could possibly be observed in this setup.

Instead let us consider an asymmetric model, in which the well frequencies differ by $\Delta\omega = \omega_B - \omega_A$ and the coupling strength mismatch between reactants and products is parameterised by $0 \leq \rho \leq 1$, in which $\rho = 1$ corresponds to the products being uncoupled from the optical cavity and $\rho = 0$ the reactants being uncoupled. Fig. 5.1 shows this setup, along with the hard-coded values of $E_A - E_B = k_B T$ and $\omega_A = 500 \text{ cm}^{-1}$.

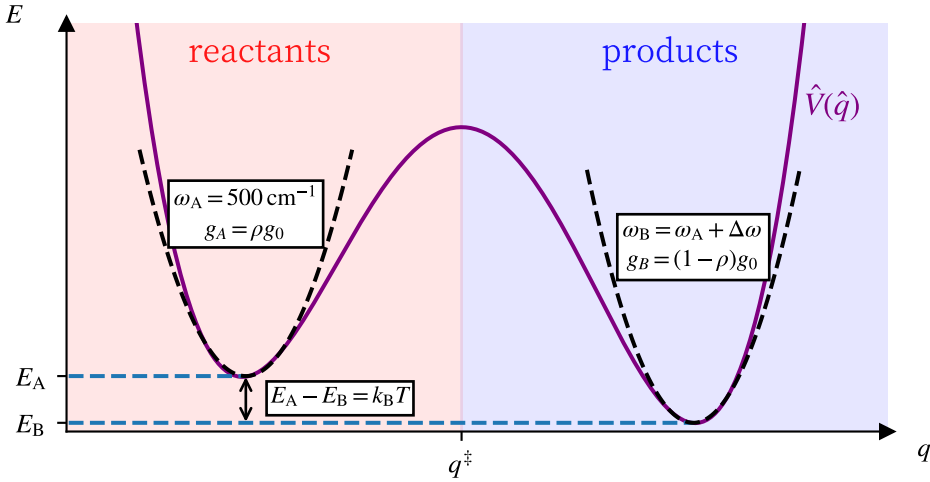


Figure 5.1: Parameterised equilibrium system setup, showing the harmonic approximations (dashed black lines) to the reaction coordinate potential $\hat{V}(q)$ (purple line) at the reactant and product minima.

We define the coupling parameter as

$$g_0 = 2\sqrt{\frac{2}{\omega_c}}\eta_c, \quad (5.52)$$

which is chosen such that when $\rho = 0.5$, the Rabi splitting of reactants is unchanged from the previous sections for a given value of η_c (the same coupling constant was used by Lindoy *et al.* in Ref. [23] and by us in Ch. 3 and Ch. 4). When ρ changes from 0 to 1, Ω_R will change, but it remains on the order of 100 cm^{-1} in all cases we shall consider, ensuring that the system remains within the regime of vibrational strong coupling.

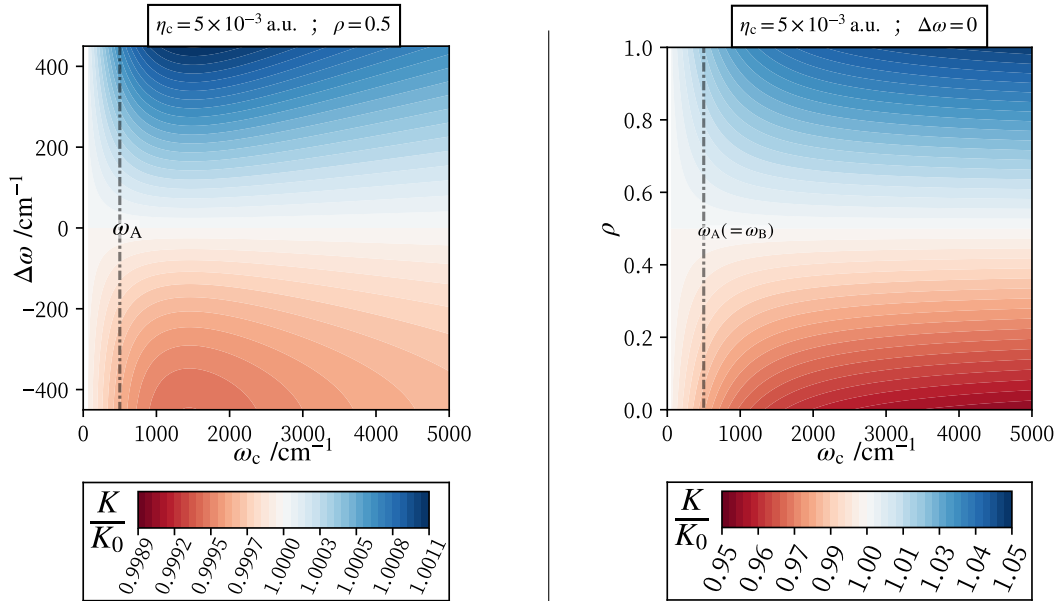


Figure 5.2: A scan over frequency miss-match (left panel) and polarity imbalance (right panel) to find conditions under which the optical cavity most affects the ratio of cavity-coupled to uncoupled equilibrium constants K/K_0 for a **single molecule reaction**.

Firstly let us consider a single molecule and probe the influence of $\Delta\omega$ and ρ on the cavity effect on the equilibrium constant. The light-matter coupling constant is fixed at its maximum value from Sec. 3.3 such that $\eta_c = 5 \times 10^{-3}$ a.u. and the temperature is set to 300 K. In the left panel Fig. 5.2, we explore the effect of changing $\Delta\omega$ whilst fixing $g_A = g_B$. For the right panel, we instead vary ρ such that $g_A \neq g_B$, for $\omega_A = \omega_B$. Both show weak effects (quantified by K/K_0) over a broad range of ω_c , with both enhancement and reduction of equilibrium constant observed. Now by selecting parameters that maximise the single molecule effect, let us see whether the observed effects survive in the collective regime. As always, we will keep $\eta_c\sqrt{N}$ constant, such that the Rabi splitting is constant as N increases.

Fig. 5.3 shows the same ‘scaling-out’ behaviour as previously observed in Fig. 4.4. Note that in preliminary tests very many possible values of $\Delta\omega$, ω_c and ρ were tested - all with the same results: any effect on single molecule equilibrium constants observed is negligible in the collective regime.

Though the derivation of Sec. 5.2 applied for a single molecular degree of freedom, the multidimensional generalisation is simple. It only requires replacing ω_A^2 and ω_B^2

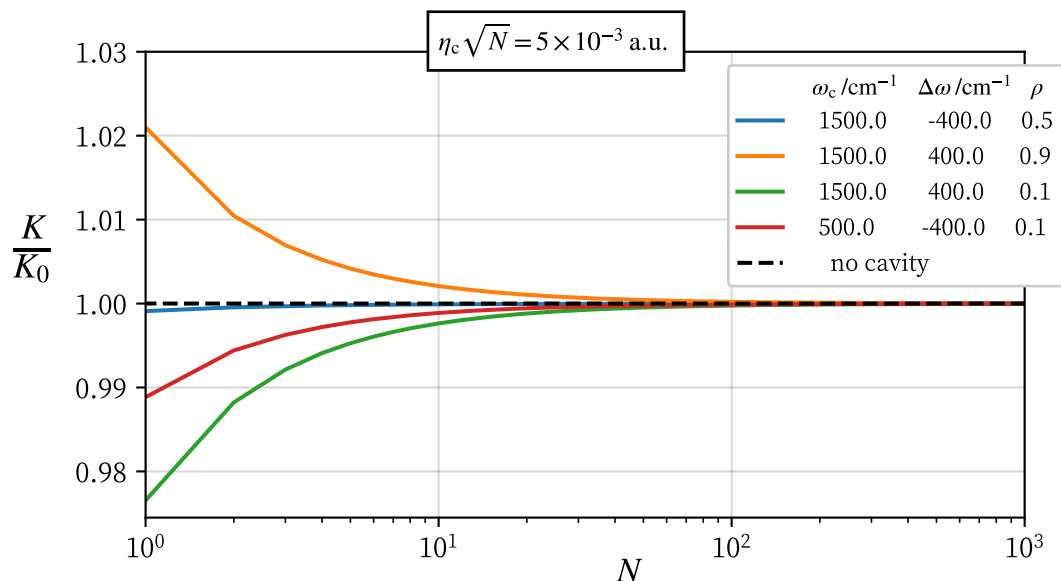


Figure 5.3: Cavity effects on the equilibrium constant ‘scale out’ as N is increased. The lines are chosen to illustrate that this is seen throughout the (very large) parameter space.

with the Hessians of the multidimensional system, and a vectorising of the coupling constants g_A and g_B . By including solvent bath degrees of freedom within each system, friction effects on the reaction coordinate could be included. In addition, a cavity loss bath could be added due to there being no direct interaction between this bath and the reaction coordinates, allowing the dark states to be ‘integrated out’, just as we have done here. When at equilibrium though, these baths will be in equilibrium with the systems they are attached to, slightly altering the effective frequency distribution of the systems but otherwise having no significant effect.

For these reasons - even if friction were to be added - the single-molecule effects would scale out in the same way as shown in Fig. 5.3, hence we will stop our analysis of equilibrium effects here. This decision is further justified by considering the results of Fig. 3.6, in which it was observed that the inclusion of friction and loss did not significantly effect the transition state theory rate of reaction relative to Yang and Cao’s results [25].

This concludes our examination of polariton chemistry. Next chapter we will summarise our findings, discussing the possible insights this thesis has given towards the understanding of chemistry under vibrational strong coupling.

6

Conclusion

In this thesis we have used various theories/methods to study the effect of vibrational strong coupling on chemical reaction dynamics. Let us firstly summarise the results of the preceding chapters:

- Ch. 3 addressed the dynamics of a single reaction coupled to the optical cavity. The origin of the rate modification observed here was found to be a dynamical recrossing effect, present only in the low-friction regime. For this reason, transition state theory was concluded to be insufficient to explain the observed effects (see Sec. 3.4).
- Ch. 4 then demonstrated that none of the effects found for the single-reaction study would survive in the limit of a macroscopic number of N reactions collectively coupled to the cavity.
- Ch. 5 turned the focus towards cavity effects on equilibria. In contrast with the previous findings, these were found to be solely quantum-mechanical. The effects observed did again however succumb to the same problem at large N , indicating that no significant change in rate or equilibrium constant would be observed for an experimentally realistic value of N .

A large, and ever growing number of theoretical studies [23, 30, 31] have now been published discussing single reactions coupled to optical cavities. The analysis in this thesis (in agreement with Ref. [32]) highlights a common problem with many of these studies: under the Pauli–Fierz Hamiltonian, the optical cavity couples to the total dipole of the system, summed over each individual reactant.

This means that when N **identical** quantum systems are collectively coupled to an optical cavity, a single linear combination of their individual dipoles couples to the cavity mode (forming the upper and lower polaritons) leaving $N-1$ dark, **completely unaffected** combinations unchanged. For this reason no effects observed for a single molecule remain in the collective regime, in agreement with our findings from Chs. 4 and 5: single molecule effects may be observed, but as N increases the dark states dominate the system’s characteristics leading to the scaling-out observed. Note that if no rates are affected, then by detailed balance, equilibrium constants also cannot be effected.

This analysis raises the question of whether there does exist some mechanism by which dark states could be modified by vibrational strong coupling. Botzung *et al.* in Ref. [33] used Markovian master equation treatment to study an ensemble of **disordered** two-level systems (each of slightly different transition frequency) collectively coupled to an optical cavity. They found that whilst still forming a lower and upper polariton, this disorder also led to hybridisation between dark states of similar energies, allowing coherent energy transportation between them, even in the thermodynamic (large N) limit. This may imply that the assumption of identical reactive systems was a shortcoming in our investigations, and that for collective effects to be observed both a quantum-mechanical treatment of systems (for proper inclusion of coherences) and disorder amongst these systems (to promote dark state mixing) is required. In addition, it may also be possible - in analogy with disorder-driven mixing - that mixing could occur between vibrational transitions of

similar energy for anharmonic potentials, if treated quantum-mechanically.

Another possible shortcoming of the present study could be the single mode approximation. The results of Figs. 3.5, 3.6 and 5.2 do not show any well defined polariton resonance, but instead effects over a large spectrum of cavity frequencies ω_c . This could imply that there are interactions between non-resonant cavity modes and reactive systems. Could it be that rate/equilibrium constant modification can only be observed as the combined interaction of all of these modes with the system?

Since it has proven so difficult to explain the rate effect, it is worth carefully analysing the existing experimental evidence for this phenomenon. There have so far been at least two failed reproductions of the motivational experimental evidence. In Ref. [34], Imperatore *et al.* found no cavity effect on the rate of cyanate ion hydrolysis despite observing the same Rabi splitting as Hiura *et al.* [35], who previously observed a 100-fold rate increase during their experiments. Also, Wiesehan and Xiong tried, and failed [36], to reproduce the 10-fold rate increase observed for ester hydrolysis of para-nitrophenyl acetate by Lather *et al.* [1], again despite observing the same Rabi splitting.

In addition to the lack of reproducibility, issues regarding measurement with optical methods have been raised. Di Virgilio *et al.* explored the cavity influence on the electro-optic response of a semiconducting perovskite coupled to resonant optical cavity [37]. Despite finding no effects on the material properties, they did find significant changes in the spectroscopic response of perovskite coupled to the cavity. Spectroscopic techniques such as monitoring the infrared transmission spectrum of higher-order cavity modes [38], or detecting the reactant/product concentration via UV/Visible spectroscopy [7], are commonly used to measure the extent of reactions occurring within optical cavities. The findings of Di Virgilio *et al.* open the possibility that the results could be purely an optical effect, and not

rate modification as reported. In addition to this, as these are ‘pump-probe’ type experiments, could it be that the measurement of reaction extent by these methods is resulting in an inadvertent pumping of the optical cavity with extra energy?

Whilst this thesis may have only shown that the Hamiltonian used is insufficient to explain observed polariton effects on reaction rates, the ubiquitous failure of other theoretical explanations could instead be seen as further evidence undermining the validity of the experimental findings. Until the speculations regarding the reproducibility of the experimental results are resolved, there is therefore no answer as to whether chemistry under vibrational strong coupling is a triumph of modern science or simply a synthetic chemist’s dream.

Bibliography

- [1] Lather, J., Bhatt, P., Thomas, A., Ebbesen, T. W. & George, J. Cavity catalysis by cooperative vibrational strong coupling of reactant and solvent molecules. *Angewandte Chemie International Edition* **58**, 10635–10638 (2019).
- [2] Nagarajan, K., Thomas, A. & Ebbesen, T. W. Chemistry under vibrational strong coupling. *Journal of the American Chemical Society* **143**, 16877–16889 (2021).
- [3] Li, T. E., Cui, B., Subotnik, J. E. & Nitzan, A. Molecular polaritonics: Chemical dynamics under strong light-matter coupling. *Annual Review of Physical Chemistry* **73**, 43–71 (2022).
- [4] Thomas, A. *et al.* Ground-state chemical reactivity under vibrational coupling to the vacuum electromagnetic field. *Angewandte Chemie International Edition* **55**, 11634–11638 (2016).
- [5] Hutchison, J. A., Schwartz, T., Genet, C., Devaux, E. & Ebbesen, T. W. Modifying chemical landscapes by coupling to vacuum fields. *Angewandte Chemie International Edition* **51**, 1592–1596 (2012).
- [6] Thomas, A. *et al.* Tilting a ground-state reactivity landscape by vibrational strong coupling. *Science* **363**, 615–619 (2019).
- [7] Pang, Y. *et al.* On the role of symmetry in vibrational strong coupling: The case of charge-transfer complexation. *Angewandte Chemie International Edition* **59**, 10436–10440 (2020).
- [8] Sau, A. *et al.* Modifying woodward–hoffmann stereoselectivity under vibrational strong coupling. *Angewandte Chemie International Edition* **60**, 5712–5717 (2021).
- [9] Vergauwe, R. M. A. *et al.* Modification of enzyme activity by vibrational strong coupling of water. *Angewandte Chemie International Edition* **58**, 15324–15328 (2019).
- [10] Lather, J. & George, J. Improving enzyme catalytic efficiency by co-operative vibrational strong coupling of water. *The Journal of Physical Chemistry Letters* **12**, 379–384 (2020).
- [11] Lawrence, J. *Path-integral methods for non-adiabatic reaction rates*. Ph.D. thesis, University of Oxford (2020).
- [12] Miller, W. H., Schwartz, S. D. & Tromp, J. W. Quantum mechanical rate constants for bimolecular reactions. *The Journal of Chemical Physics* **79**, 4889–4898 (1983).
- [13] Parrinello, M. & Rahman, A. Study of an F center in molten KCl. *The Journal of Chemical Physics* **80**, 860–867 (1984).
- [14] Craig, I. & Manolopoulos, D. Quantum statistics and classical mechanics: real time correlation functions from ring polymer molecular dynamics. *The Journal of Chemical Physics* **121**, 3368–3373 (2004).
- [15] Dirac, P. A. M. The quantum theory of the emission and absorption of radiation. *Proceedings of the Royal Society of London Series A* **114**, 243–265 (1927).
- [16] Craig, I. R. & Manolopoulos, D. E. Chemical reaction rates from ring polymer molecular dynamics. *The Journal of Chemical Physics* **122**, 034102 (2005).
- [17] Lawrence, J. E. & Manolopoulos, D. E. Path integral methods for reaction rates in complex systems. *Faraday Discussions* **221**, 9–29 (2019).
- [18] Habershon, S., Manolopoulos, D. E., Markland, T. E. & Miller, T. F. Ring-polymer molecular dynamics: Quantum effects in chemical dynamics from classical trajectories in an extended phase space. *Annual Review of Physical Chemistry* **64**, 387–413 (2013).
- [19] Craig, I. R. & Manolopoulos, D. E. A refined ring polymer molecular dynamics theory of chemical reaction rates. *The Journal of Chemical Physics* **123**, 034102 (2005).

- [20] Eyring, H. The activated complex in chemical reactions. *The Journal of Chemical Physics* **3**, 107–115 (1935).
- [21] Kramers, H. A. Brownian motion in a field of force and the diffusion model of chemical reactions. *Physica* **7**, 284–304 (1940).
- [22] Topaler, M. & Makri, N. Quantum rates for a double well coupled to a dissipative bath: Accurate path integral results and comparison with approximate theories. *The Journal of Chemical Physics* **101**, 7500–7519 (1994).
- [23] Lindoy, L. P., Mandal, A. & Reichman, D. R. Quantum dynamical effects of vibrational strong coupling in chemical reactivity. *Nature Communications* **14**, 2733 (2023).
- [24] Cohen-Tannoudji, C., Grynberg, G. & Dupont-Roc, J. *Photons and atoms: Introduction to quantum electrodynamics* (Wiley, 1997).
- [25] Yang, P. Y. & Cao, J. Quantum effects in chemical reactions under polaritonic vibrational strong coupling. *Journal of Physical Chemistry Letters* **12**, 9531–9538 (2021).
- [26] Li, T. E., Subotnik, J. E. & Nitzan, A. Cavity molecular dynamics simulations of liquid water under vibrational ultrastrong coupling. *Proceedings of the National Academy of Sciences* **117**, 18324–18331 (2020).
- [27] Mandal, A., Vega, S. M. & Huo, P. Polarized Fock states and the dynamical Casimir effect in molecular cavity quantum electrodynamics. *Journal of Physical Chemistry Letters* **11**, 9215–9223 (2020).
- [28] Mandal, A., Li, X. & Huo, P. Theory of vibrational polariton chemistry in the collective coupling regime. *The Journal of Chemical Physics* **156**, 014101 (2022).
- [29] Li, T. E., Nitzan, A. & Subotnik, J. E. On the origin of ground-state vacuum-field catalysis: Equilibrium consideration. *The Journal of Chemical Physics* **152**, 234107 (2020).
- [30] Anderson, M. C., Woods, E. J., Fay, T. P., Wales, D. J. & Limmer, D. T. On the mechanism of polaritonic rate suppression from quantum transition paths (2023). ArXiv: 2304.13024.
- [31] Philbin, J. P., Wang, Y., Narang, P. & Dou, W. Chemical reactions in imperfect cavities: enhancement, suppression, and resonance (2022). ArXiv: 2206.00852.
- [32] Campos-Gonzalez-Angulo, J. A., Poh, Y. R., Du, M. & Yuen-Zhou, J. Swinging between shine and shadow: Theoretical advances on thermally-activated vibropolaritonic chemistry (a perspective) (2023). ArXiv: 2212.04017.
- [33] Botzung, T. *et al.* Dark state semilocalization of quantum emitters in a cavity. *Physical Review B* **102**, 144202 (2020).
- [34] Imperatore, M., Asbury, J. & Giebink, N. Reproducibility of cavity-enhanced chemical reaction rates in the vibrational strong coupling regime. *The Journal of Chemical Physics* **154**, 191103 (2021).
- [35] Hiura, H., Shalabney, A. & George, J. Vacuum-field catalysis: Accelerated reactions by vibrational ultra strong coupling (2018). Chemrxiv: 7234721.
- [36] Wiesehan, G. D. & Xiong, W. Negligible rate enhancement from reported cooperative vibrational strong coupling catalysis. *The Journal of Chemical Physics* **155**, 241103 (2021).
- [37] Di Virgilio, L. *et al.* Controlling the electro-optic response of a semiconducting perovskite coupled to a phonon-resonant cavity. [Unpublished manuscript].
- [38] Hirai, K., Takeda, R., Hutchison, J. A. & Uji-i, H. Modulation of Prins cyclization by vibrational strong coupling. *Angewandte Chemie International Edition* **59**, 5332–5335 (2020).
- [39] Korol, R., Bou-Rabee, N. & Miller, T. F. Cayley modification for strongly stable path-integral and ring-polymer molecular dynamics. *The Journal of Chemical Physics* **151**, 124103 (2019).
- [40] Baczewski, A. D. & Bond, S. D. Numerical integration of the extended variable generalized Langevin equation with a positive Prony representable memory kernel. *The Journal of Chemical Physics* **139**, 241103 (2013).

Appendices

A

The Cayley Propagator

When numerically integrating harmonic equations of motion, it is usually a rule of thumb that the time-step δt must be sufficiently small such that,

$$\delta t \leq \frac{0.1\pi}{\omega_{\max}}, \quad (\text{A.1})$$

in which ω_{\max} is the maximum frequency of the system. When integrating the equations of motion of a ring polymer, this results in an annoying feature for simulations with large numbers of beads, as high frequency normal mode components require very small time steps for integration to remain stable. This appendix describes a fix to this problem that is very effective for the special (system + bath) case considered in this thesis.

A.1 Cayley Propagator

In this description, a single molecular degree of freedom (DOF), connected to its own Caldeira-Leggett bath will be considered. Multidimensional generalisation is as straightforward as adding another index to all variables. Also, for simplicity we use mass-scaled coordinates and momenta. The structuring of the variables is as follows.

- There are n_f physical degrees of freedom. The first index corresponds to the

molecular DOF, the remaining indices from 2 to n_f correspond to those of a discretised bath with $n_f - 1$ modes (see Appendix B).

- ω_i and c_i hold the discretised bath frequencies/coupling strengths, each in an array of size n_f . The index from 2 to n_f hold the information for each the $n_f - 1$ bath modes. The first index is fixed such that $c_1 = \omega_1^2$, such that the summations in Eq. (A.4) may be over all molecular DOFs, simplifying notation.
- The phase-space variables p_{ij} and q_{ij} have two indices. The i index runs from 1 to n_f and corresponds to the physical DOFs. The j index is the ring polymer bead index. It runs from 1 to n_b , the number of ring polymer beads.
- $\omega_n = \frac{1}{\beta_n \hbar}$ is the ring polymer spring frequency.

Using this structure, let us setup the ring polymer Hamiltonian of a generic 1-dimensional system coupled to a bath of harmonic oscillators such that,

$$H(\{p_{ij}\}, \{q_{ij}\}) = H_0(\{p_{ij}\}, \{q_{ij}\}) + V(\{q_{1j}\}). \quad (\text{A.2})$$

Here

$$V(\{q_{1j}\}) = \sum_{j=1}^{n_b} V(q_{1j}), \quad (\text{A.3})$$

the potential energy experienced by the molecular system (which is not necessarily harmonic, and hence separated from H_0) and

$$H_0(\{p_{ij}\}, \{q_{ij}\}) = \sum_{i=1}^{n_f} \sum_{j=1}^{n_b} \left(\frac{p_{ij}^2}{2} + \underbrace{\frac{1}{2} \omega_n^2 (q_{ij} - q_{ij+1})^2}_{\text{Ring polymer springs } V_{\text{rp}}} + \underbrace{\frac{1}{2} \omega_i^2 \left(q_{ij} - \frac{c_i}{\omega_i^2} q_{1j} \right)^2}_{\text{System-bath interactions } V_{\text{sb}}} \right). \quad (\text{A.4})$$

As the ring polymer potential is the same for all i and the system bath potential for all j , it is useful to define the ring polymer Hessian

$$(\mathbf{V}_{\text{rp}}'')_{jj'} = \frac{\partial^2 V_{\text{rp}}}{\partial q_{ij} \partial q_{ij'}}, \quad (\text{A.5})$$

and the system-bath Hessian

$$(\mathbf{V}_{\text{sb}}'')_{ii'} = \frac{\partial^2 V_{\text{sb}}}{\partial q_{ij} \partial q_{i'j}}, \quad (\text{A.6})$$

as they allow us to re-write Eq. (A.4) in terms of n_f by n_b matrices \mathbf{p} and \mathbf{q} as

$$H_0(\mathbf{p}, \mathbf{q}) = \frac{1}{2} \left(\text{Tr}\{\mathbf{p}^\top \mathbf{p}\} + \text{Tr}\{\mathbf{q} \mathbf{V}_{\text{rp}}'' \mathbf{q}^\top\} + \text{Tr}\{\mathbf{q}^\top \mathbf{V}_{\text{sb}}'' \mathbf{q}\} \right). \quad (\text{A.7})$$

Let us define the unitary transformations that diagonalise \mathbf{V}_{rp}'' and \mathbf{V}_{sb}'' such that,

$$\mathbf{V}_{\text{rp}}'' = \mathbf{U}_{\text{rp}} \boldsymbol{\omega}_{\mathbf{k}}^2 \mathbf{U}_{\text{rp}}^\top, \quad (\text{A.8})$$

in which $\boldsymbol{\omega}_{\mathbf{k}}^2$ is a diagonal matrix of eigenvalues ω_k^2 and

$$\mathbf{V}_{\text{sb}}'' = \mathbf{U}_{\text{sb}} \boldsymbol{\omega}_{\mathbf{l}}^2 \mathbf{U}_{\text{sb}}^\top, \quad (\text{A.9})$$

in which $\boldsymbol{\omega}_{\mathbf{l}}^2$ is a diagonal matrix of eigenvalues ω_l^2 . Therefore by two unitary transforms, Eq. (A.4) can be re-written as

$$H_0(\{\tilde{p}_{lk}\}, \{\tilde{q}_{lk}\}) = \sum_{l=1}^{n_f} \sum_{k=1}^{n_b} \left(\frac{\tilde{p}_{lk}^2}{2} + \frac{1}{2} \underbrace{(\omega_l^2 + \omega_k^2)}_{\omega_{lk}^2} \tilde{q}_{lk}^2 \right). \quad (\text{A.10})$$

where

$$\tilde{q}_{lk} = \sum_{i=1}^{n_f} \sum_{j=1}^{n_b} (\mathbf{U}_{\text{sb}})_{il} q_{ij} (\mathbf{U}_{\text{rp}})_{jk}, \quad (\text{A.11})$$

or (equivalently)

$$\tilde{\mathbf{q}} = \mathbf{U}_{\text{sb}}^\top \mathbf{q} \mathbf{U}_{\text{rp}}. \quad (\text{A.12})$$

The momentum is transformed similarly. For the element lk in this new basis, the equations of motion generated by the Hamiltonian can be written in matrix form as

$$\frac{d}{dt} \underbrace{\begin{pmatrix} \tilde{p}_{lk} \\ \tilde{q}_{lk} \end{pmatrix}}_{\tilde{\mathbf{x}}_{lk}(t)} = \underbrace{\begin{pmatrix} 0 & -\omega_{lk}^2 \\ 1 & 0 \end{pmatrix}}_{\mathbf{A}_{lk}} \begin{pmatrix} \tilde{p}_{lk} \\ \tilde{q}_{lk} \end{pmatrix} \quad (\text{A.13})$$

which can be numerically integrated using

$$\tilde{\mathbf{x}}_{lk}(t+\delta t) = e^{\mathbf{A}_{lk} \delta t} \tilde{\mathbf{x}}_{lk}(t) \quad (\text{A.14})$$

The Cayley propagator uses an approximation to the exponential, which is more stable for larger time-steps when used within the split-operator scheme in Eq. (A.17) below [39]. The approximation itself is

$$e^{\mathbf{A}_{lk}\delta t} \approx \left(\mathbb{1} - \mathbf{A}_{lk} \frac{\delta t}{2} \right)^{-1} \left(\mathbb{1} + \mathbf{A}_{lk} \frac{\delta t}{2} \right). \quad (\text{A.15})$$

We can now insert the definition of \mathbf{A}_{lk} to obtain an analytical expression for the propagator,

$$\begin{aligned} e^{\mathbf{A}_{lk}\delta t} &\approx \begin{pmatrix} 1 & \omega_{lk}^2 \frac{\delta t}{2} \\ -\frac{\delta t}{2} & 1 \end{pmatrix}^{-1} \begin{pmatrix} 1 & -\omega_{lk}^2 \frac{\delta t}{2} \\ \frac{\delta t}{2} & 1 \end{pmatrix} \\ &= \frac{1}{1 + c_{lk}} \begin{pmatrix} 1 - c_{lk} & -\omega_{lk}^2 \delta t \\ \delta t & 1 - c_{lk} \end{pmatrix}, \end{aligned} \quad (\text{A.16})$$

where we have defined $c_{lk} = \frac{\omega_{lk}^2 \delta t^2}{4}$. With this propagator we can apply the Liouvillian \mathcal{L}_0 corresponding to H_0 , ensuring that the integration is stable. To integrate the equations of motion generated by H though, the external potential must also be taken into account. We do this by symmetrically splitting the integration such that,

$$e^{\mathcal{L}\delta t} \approx e^{\mathcal{L}_V \frac{\delta t}{2}} \underbrace{e^{\mathcal{L}_0 \delta t}}_{\text{Cayley}} e^{\mathcal{L}_V \frac{\delta t}{2}}. \quad (\text{A.17})$$

With the Cayley propagator, integration is done in the normal mode coordinates (tildes) of the phase-space variables. For \mathcal{L}_V though, the potential must be evaluated using the physical coordinates (no tilde). As the external potential is only applied to q_{1j} , we only need to transform this component, calculate the change in the conjugate momenta δp_{1j} over each half time step, then transform back to the normal mode representation.

To achieve $e^{\mathcal{L}_V \frac{\delta t}{2}}$, firstly obtain $\{q_{1j}\}$ via

$$q_{1j} = \sum_{l=0}^{n_f-1} \sum_{k=0}^{n_b-1} (\mathbf{U}_{\text{sb}})_{1l} \tilde{q}_{lk} (\mathbf{U}_{\text{rp}})_{jk}, \quad (\text{A.18})$$

then using Hamilton's equations calculate

$$\delta p_{1j} = -\frac{\delta t}{2} V'(q_{1j}), \quad (\text{A.19})$$

then transform back δp and apply to the system

$$\tilde{p}_{lk} \leftarrow \tilde{p}_{lk} + \sum_{j=1}^{n_b} (\mathbf{U}_{\mathbf{sb}})_{lj} \delta p_{1j} (\mathbf{U}_{\mathbf{rp}})_{jk}. \quad (\text{A.20})$$

This algorithm allows fast and stable integration of the equations of motion of any (adiabatic) ring polymerised system, in which the majority of the interactions are harmonic (as they are in the system-bath model).

B

Bath Discretisation and GLEs

The system–bath model is used to model the interactions between a system and its environment, for example a solvent. In this appendix, we describe how the baths were constructed. For each bath, the spectral density $J(\omega)$ (see Sec. 2.4) was discretised into a sum over a finite number of modes,

$$J_n(\omega) = \frac{\pi}{2} \sum_{i=1}^n \frac{c_i^2}{\omega_i} \delta(\omega - \omega_i) \quad (\text{B.1})$$

B.1 Discrete Ohmic Baths

The results of section 2.6 were reproduced from [16]. In this paper an Ohmic bath was used with spectral density of the form

$$J_{\text{Ohm.}}(\omega) = \eta \omega e^{-\omega/\gamma}, \quad (\text{B.2})$$

where the cutoff frequency γ and solvent strength η is that of the bath in question. The Ohmic bath was discretised into the form in Eq. (B.1) through the same scheme as in [16] which is

$$\omega_i = -\gamma \ln \left(\frac{i - 1/2}{n} \right) \quad c_i = \omega_i \left(\frac{2\eta\gamma}{n\pi} \right)^{\frac{1}{2}}, \quad (\text{B.3})$$

for $i = 1, 2, \dots, n$. For this model, $n = 9$ was required for graphical convergence (see abstract of Ref. [16]).

B.2 Discrete Debye baths

For the remainder of the thesis (Chapter 3 onwards) Debye baths were used. For this,

$$J_{\text{Deb.}}(\omega) = \eta\omega \frac{\gamma^2}{\omega^2 + \gamma^2}, \quad (\text{B.4})$$

where η is the solvent strength and $\tau = 1/\gamma$ is timescale corresponding to the Debye spectral density. Now the discretisation scheme to assign c_i and ω_i for a given number of bath modes n is

$$\omega_i = \gamma \tan\left(\frac{(i - 1/2)\pi}{2n}\right) \quad c_i = \omega_i \left(\frac{\eta\gamma}{n}\right)^{\frac{1}{2}}. \quad (\text{B.5})$$

for $i = 1, 2, \dots, n$.

B.3 Generalised Langevin Equations (GLEs)

For the classical simulations of Chapter 4, instead of including discretised baths, GLEs were employed in order to improve computational efficiency. For the Debye spectral density there is an efficient algorithm in terms of a Prony series which follows Ref. [40]. This is the same algorithm used by Lindoy *et al.* in Ref. [23], the implementation of which is discussed in their appendix.

C

Model Parameters

For Ch. 2, the model parameters used were the same as in Refs. [22, 16]. As this model is not the main focus of this thesis they will not be included here.

For Chs. 3 and 4 (for the same model used in Fig. S2 of the supplementary information of Ref.[23]) the following solvent cutoff parameters, double-well parameters and timestep were used,

γ_L	γ_s	ω_b	E_b	dt
1000 cm^{-1}	200 cm^{-1}	500 cm^{-1}	2000 cm^{-1}	20 au

For Chs. 3 and 5 the temperature was set to 300 K, for Ch. 4 however, the temperature was set to 500 K. All other information for the parameters used in Ch. 5 can be found in Sec. 5.3.

C.1 Convergence information: Flux-Side Correlation

For all simulations, the number of bath modes, plateau time and number of trajectories was the same.

n_L	n_S	t_p	$n_{\text{traj.}}$
200	200	1200 fs	2×10^5

These were sufficient to converge the results shown in the plots.

C.2 Convergence information: Direct Simulation

For the direct simulation, firstly the reactants were equilibrated for 2500 fs, from an initial condition of all coordinates in the center of the reactant well, with their momenta sampled from the Maxwell–Boltzmann distribution. The system’s coordinates and momenta was then recorded at 100 fs intervals, until enough samples had been taken. Then each snapshot was simulated for 5000 fs in stage 2. The number of trajectories in the main part of Fig. 4.4 were

$n_{\text{sys.}}$	1	5	10	25	50
$n_{\text{traj.}}$	1×10^5	1×10^5	1×10^5	5×10^4	5×10^4

For the inset in Fig. 4.4, the number of trajectories was calculated as $n_{\text{traj.}} = 10^5 / \sqrt{n_{\text{sys.}}}$.

D

Outside-cavity Equilibria

If Eq. (5.47) is to be true it must reduce to the outside-cavity equilibrium constant K_0 when the coupling constants $g_A = g_B = 0$. Looking at the Hessian from Eq. (5.43) by which $\{\lambda_{r1}, \lambda_{r2}, \lambda_{r3}\}$ are obtained, all terms containing r are multiplied by either g_A or g_B . Therefore when uncoupled, the eigenvalues will not have any r dependence. This means the bright-state factor $B(r)$ is now a constant and as such may be cancelled such that the uncoupled equilibrium constant

$$K_{\text{uncoup.}} = \frac{\sum_{r=0}^N \binom{N}{r} (N-r) K_0^{-r}}{\sum_{r=0}^N \binom{N}{r} r K_0^{-r}}. \quad (\text{D.1})$$

Looking at the denominator,

$$\begin{aligned} \sum_{r=0}^N \binom{N}{r} r K_0^{-r} &= K_0^{-1} \sum_{r=0}^N \binom{N}{r} r K_0^{-r+1} \\ &= K_0^{-1} \sum_{r=1}^N \frac{N!}{r!(N-r)!} r K_0^{-r+1} \\ &= K_0^{-1} \sum_{r=1}^N \frac{N!}{(r-1)!(N-(r-1))!} (N-(r-1)) K_0^{-(r-1)}. \end{aligned} \quad (\text{D.2})$$

Now let us introduce $r' = r - 1$, such that

$$\begin{aligned}
\sum_{r=0}^N \binom{N}{r} r K_0^{-r} &= K_0^{-1} \sum_{r'=0}^{N-1} \frac{N!}{(r')!(N-r')!} (N-r') K_0^{-r'} \\
&= K_0^{-1} \sum_{r'=0}^N \frac{N!}{(r')!(N-r')!} (N-r') K_0^{-r'} \\
&= K_0^{-1} \sum_{r=0}^N \binom{N}{r} (N-r) K_0^{-r},
\end{aligned} \tag{D.3}$$

in which the prime was removed in the last step (as labelling was arbitrary). Inserting this back into Eq. (D.1),

$$\begin{aligned}
\frac{\sum_{r=0}^N \binom{N}{r} (N-r) K_0^{-r}}{\sum_{r=0}^N \binom{N}{r} r K_0^{-r}} &= \frac{\sum_{r=0}^N \binom{N}{r} (N-r) K_0^{-r}}{K_0^{-1} \sum_{r=0}^N \binom{N}{r} (N-r) K_0^{-r}} \\
&= K_0 \\
\therefore K_{\text{uncoup.}} &= K_0.
\end{aligned} \tag{D.4}$$